Adaptive Synchronization of PR Controllers in Grid-connected Inverters

by

Kamyar Seifi

B.Sc., Ferdowsi University, 2013

Thesis Submitted in Partial Fulfillment of the
Requirements for the Degree of
Master of Applied Science

in the
School of Mechatronic Systems Engineering
Faculty of Applied Science

SIMON FRASER UNIVERSITY
Spring 2017

Approval

Name:	**Kamyar Seifi**
Degree:	**Master of Applied Science (Engineering)**
Title:	***Adaptive Synchronization of PR Controllers in Grid-connected Inverters***
Examining Committee:	**Chair:** Faranak Farzan Assistant Professor

Mehrdad Moallem
Senior Supervisor
Professor _____

Jiacheng (Jason) Wang
Supervisor
Assistant Professor _____

Amr Marzouk
Internal Examiner
Lecturer
School of Mechatronic Systems
Engineering
Simon Fraser University _____

Date Defended: 1 May 2017

Abstract

This thesis focuses on the development of control schemes for single-phase Voltage Source Inverters (VSIs) to ensure that they meet standards for injection of power into the utility grid. For instance, conventional controllers fail to accurately control power flow if there are fluctuations in the grid frequency. Also they fail to provide high quality output currents if the grid voltage is distorted. The aim of this thesis is to address the above problems while adhering to technical standards for interconnected renewable energy systems. For synchronization of the inverter, a closed-loop filter based on the Internal Model Principle (IMP) was developed and its performance was analyzed in response to frequency variations. To this end, we utilized the perturbation-based extermum seeking algorithm to minimize the error and estimate the grid frequency. The designed adaptive controller and filter can estimate grid frequency and achieve a high Power Factor (PF). The effect of harmonic distortion on the control system was investigated and the control scheme was modified to provide low Total Harmonic Distortion (THD) output current. Furthermore, the effect of the DC-link ripple on the PI voltage control loop is analyzed and the control system was modified to attenuate the unwanted third harmonic component in the output current. Simulations were performed using Matlab/Simulink and the digital controller was implemented using Matlab Embedded Coder. A power electronics prototype was built and used to validate the performance of the controller. Based on experimental results, the controller successfully regulates the output power if the grid frequency changes. Also it is able to provide high quality current if the grid is polluted with unwanted harmonic components.

Keywords: Adaptive PR, FLL, Perturbation Extremum Seeking, Polluted Grid

Table of Contents

List of Tables

List of Figures

Chapter 1

Introduction

Renewable Energy Growth

Due to limited availability of fossil fuel resources and increased intensity in world's population, energy demands of the future decades should and is likely to be met with alternative energy resources. Recently, due to technological advancements and reduction in renewable energy production cost, the capacity of renewable energy resources have increased significantly and is continuing to do so.

According to a report provided by US department of energy [1], the production cost of distributed solar power was reduced by 54% and the production cost of utility solar power was reduced by 64% from 2008 to 2015. As shown in [1], by reduction in the cost of PV power generation, the energy production capacity was increased to more than 10 GW from 2008 to 2015 for both utility-scale and distributed PV generations. Although their speed of growth is slow and the price of PV power generation is more expensive than coal and even than the wind energy, but according to [2], [3], the solar energy may beat the price of coal in the next decade. Just recently SolarCity, a renweable energy company, was able to power the Ta'u island with 600 resident, purely from micro-grid solar energy and batteries [4].

1.1 Shift to Distributed Networks: Micro-Grids

To deliver the power generated by renewable energy resources to the utility grid in appropriate and reliable format, power converter circuits are employed which connect energy production resources to utility grid. In this section, power converter configurations that are used for connecting PV generation systems to the utility grid are discussed and reviewed.

Single-Stage Central Power Converters

In this traditional configuration, PV panels are connected in series (called string) in order to provide high output voltage. To provide higher power capacity, the strings are connected in parallel via diodes in order to avoid circulation through parallel strings. The PV panels in this configuration are connected to a single-stage central inverter which injects the produced power into the grid as it is shown in Fig 1.1(a).

Generally, the tasks associated with power converters used in PV power generation systems can be categorized as follows

- *At input*: Gather maximum available power from the PV panels by controlling the panel's operating point via Maximum Power Point Tracking (MPPT) algorithms. MPPT is automatic control technique used to set the biasing point of power interfaces to achieve maximum power from them during various conditions [5].
- *At output*: Synchronize inverter with the grid to achieve maximum Power Factor (PF). Furthermore, ensure the quality of the injected power to the grid (Low THD).

The main problem associated with this configuration is poor energy harvesting. Since the central inverter is responsible for MPPT control of all the panels connected to it, each PV panel might not operate at the maximum power point and there might be mismatches between panels. The mismatch between panels can occur due to partial shading (cloud over a segment of panels), or manufacturing variations between panels [6], [7]. Other drawbacks include losses in the string diodes. Furthermore, the non-modular structure of this configuration makes the power generation dependent to reliable operation of the central power converter. If any fault happens in this converter, it affects all of the panels and thus the whole power generation. Reduced version of this configuration includes only one string connected to the inverter rather than parallel combination of multiple strings. This configuration eliminates the losses from string diodes since the diodes are not required anymore as shown in Fig 1.1(b).

Two-stage Power Converters

To improve the energy harvesting problem of central inverter configuration, two stage configurations can be used. In this design, each panel has a dedicated DC/DC power converter responsible for MPPT control and maximum energy harvesting. A DC/AC converter is employed in the second stage which is responsible for synchronizing the output power with the grid and ensuring its quality.

In this configuration, the mismatch between panels does not limit maximum energy harvesting since MPPT control is performed for each panel by its dedicated DC/DC converter. Also the design seems to be more modular than the central configuration despite the fact

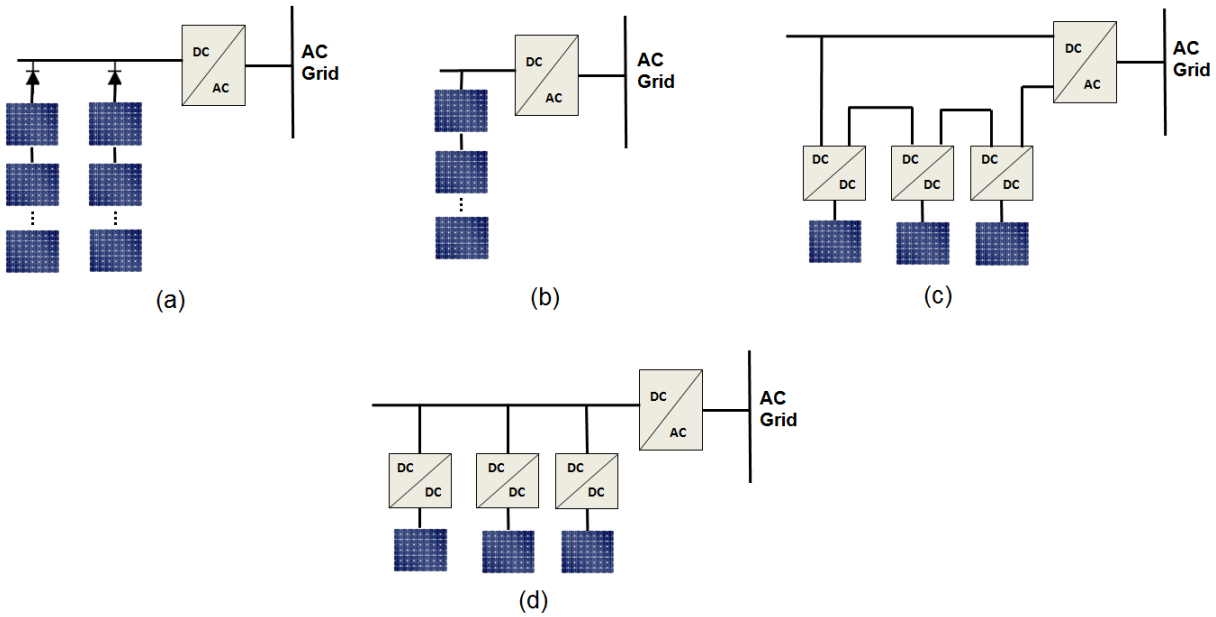

Figure 1.1: Traditional grid-tie PV configurations: (a) Parallel strings connected to a single stage central inverter (b) One string connected to a single stage central inverter (c)Two stage low voltage DC/DC converters in series (d)Two stage high voltage DC/DC converters in parallel

that it still utilizes a centralized DC/AC converter. If the output of DC/DC converter has low output voltage, thus sufficient number of them are connected in series before connecting to the inverter as shown in Fig 1.1(c). If the output of DC/DC converter has sufficiently high output voltage before connected to the inverter, DC/DC converters are connected in parallel before connecting to the central DC/AC converter as shown in Fig 1.1(d).

Furthermore, Since only one DC/AC converter is employed in this configuration, any fault associated with this converter will affect all DC/DC converters and all the panels.

Two-stage Microinverters

AC modules or micro-inverters have become a trend in recent years [6], [7]. In this structure, each PV panel is connected to a dedicated DC/DC and a DC/AC converters which work independent of other PV panels. The PV panels and their dedicated micro-inverters can connect in parallel to increase the production capacity. In this configuration, power electronics have moved closer to each panel. Consequently, the power generation is forced to become fully distributed. In this structure, since power generation resources work independent from each other, they are less likely to be affected by the failures happens in one generation system. This structure has high energy harvesting and each panel will operate at the maximum power point since each micro-inverter has a dedicated DC/DC converter

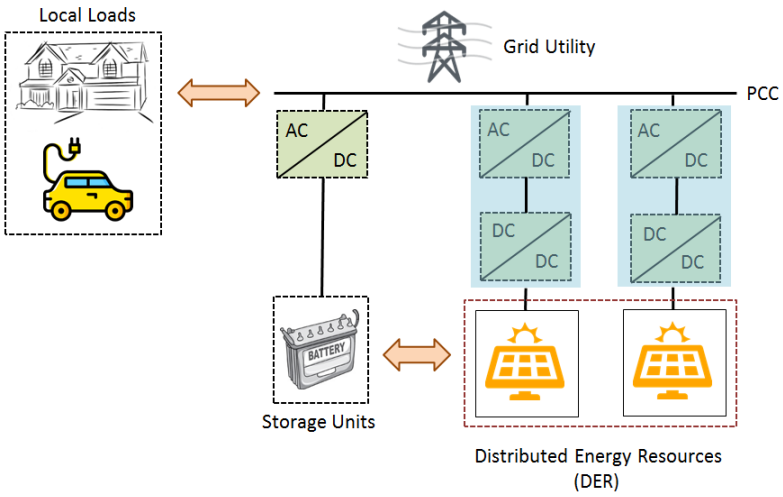

Figure 1.2: Simple diagram of a micro-grid, including renewable energy resources, storage units, local loads

with MPPT control. Furthermore, modularity in this configuration makes the scale of power generation more flexible.

Being modular and distributed makes this architecture appealing for local and small scale power generations. This system can power their own local loads such as in residential places while connected to the utility grid. These new local generation tiers, so often called micro-grids, have the ability to disconnect from the utility grid (in case of instability) and serve power to the local loads uninterrupted. The disconnected operation of the micro-grids is called *islanding mode*. Also micro-grids with renewable energies makes the transfer of power to remote areas possible. A basic diagram of a micro-grid is demonstrated in Fig 1.2.

Table 1.1: IEEE 1547 maximum current distortion [9]

Harmonics	h<11	11≤h<17	17≤h<23	...	h≥35	THD
Percent(%)	4.0	2.0	1.5	...	0.3	5.0

1.2 Micro-Grid Integration Challenges

As the capacity of renewable power generation is increased, electrical power generation systems are moving from a unidirectional central systems to multi-directional disritubed systems [10]. Thus, new policies should be employed to ensure stability and proper function of the distributed network. Power generated by PV panels is dependent on environmental conditions such as shading (due to weather condition) which decrease produced power effectively. Connecting or disconnecting each power generator from the grid affects the voltage and frequency of the electrical grid [10]. However, to maintain stability of the grid, it's voltage and frequency must remain fairly constant [10].

To ensure stability of the grid, regulatory standards such as IEEE 1547 standard are established [9]. IEEE 1547 requires the local power generation tiers to disconnect from the grid whenever the grid's voltage or frequency are above or below a pre-determined level. It also requires the Total Harmonics Distortion (THD) of the output current to be below a pre-determined level as shown by Table 1.1.

According to [10], advanced functionality of the inverters can address some of the stability challenges of the grid. Inverters are able to stay connected to the grid during small disturbances and respond appropriately to short-term events. This is often called *riding through* disturbances and can help the stability of grid by performing actions such as reactive power injection. For riding through disturbances, control systems employed in the inverters should be able to work properly during abnormal conditions and ensure the quality of injected power into the grid.

1.3 Thesis Objectives

This thesis tackles problems of a single-phase grid-tied inverter controller during grid abnormalities, particularly frequency/harmonic distortions and propose new control systems which act appropriately and adhere to the regulatory standards.

The objective of this thesis is outlined as follows

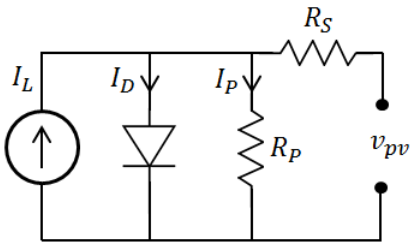

Figure 1.3: Circuit model of PV cell.

- *Response to frequency fluctuations*: Synchronization unit, filters and controllers employed in the control scheme should be able to adapt to the grid frequency variations. Otherwise control scheme might fail and might not work correctly.

- *Response to polluted grid*: Depending on the structure of inverter control scheme, harmonics presented in a polluted grid might reduce the quality of the produced power significantly. Control structure must be able to eliminate any additional harmonics that might be presented in the grid.

1.4 PV Power Generation Systems: Overview

In the following subsections, main components which are used in PV power generation systems are briefly described. This includes Photovoltaics, DC/DC converters and MPPT control, Voltage Source Inverters (VSIs) and modulation schemes. Control systems used for synchronization of inverters are studied in next chapter of this thesis.

1.4.1 Photovoltaics

Photovoltaics cells, as the main part of the PV power generation system, convert the radiance of the sun to electricity. A PV module is the combination of PV cells in different series or parallel structures [6]. Modules employed for grid-connected systems typically contain 60 to 72 solar cells [8]. Among different technologies are used to create PV modules, crystalline-silicon technology account for major PV panels capacity [8]. Nominal efficiency of PV module is almost 20% [8].

For understanding the relation between PV cell's current and voltage (I/V curve), photovoltaic cells are usually modeled by a circuit which is demonstrated in Fig 1.3. As it can be seen, generated electricity is modeled by a current source. The P-N junction of PV cell is modeled by a diode and losses are modeled by parallel and series resistances [8]. Value of the current source is proportional to amount of solar radiance. Current through the diode can be calculated by schottky diode equations.

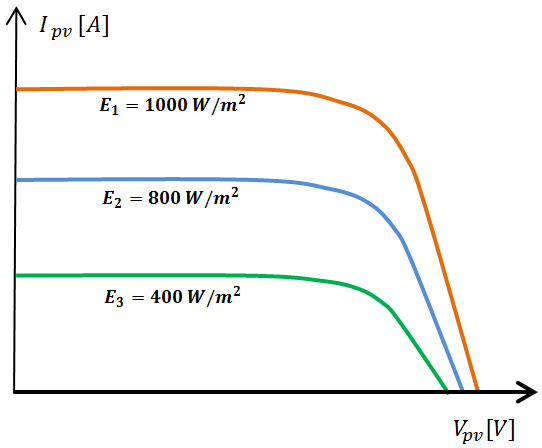

Figure 1.4: I/V characteristic curve of a PV cell in response to different light intensities

The overall I/V characteristic of a photovoltaic cell is described as follows

$$i_{pv} = I_L - I_D - I_P \tag{1.1}$$

where I_L is the current due to solar radiance, I_D is current going through the diode and I_P is the current going through the parallel shunt resistor. The values of I_D and I_P are calculated as follows

$$I_P = \frac{v_{pv} + R_s i_{pv}}{R_p} \tag{1.2}$$

$$I_D = I_s(e^{\frac{v_{pv}+i_{pv}R_s}{nV_T}} - 1) \tag{1.3}$$

In (1.3), n is the ideality factor, I_s is saturation current and V_T is diode junction thermal voltage which is calculated as follows

$$V_T = \frac{kq}{T} \tag{1.4}$$

In (1.4), k is the Boltzmann's constant ($8.617 \times 10^{-5} eV/K$), T is the temperature in Kelvin and q is the charge of an electron ($1.602 \times 10^{-19} C$).

The I/V characteristic is demonstrated at Fig 1.4. As it can be seen, for most of the operating region, PV current remains the same. Thus, the cell acts as current source. The value of the current increases as the external radiance increases [8].

Operating point of the PV module is dependent on its load, whether a passive element or an active circuit. As it is shown in Fig 1.4, at short circuit point $V_{pv} = 0$, maximum

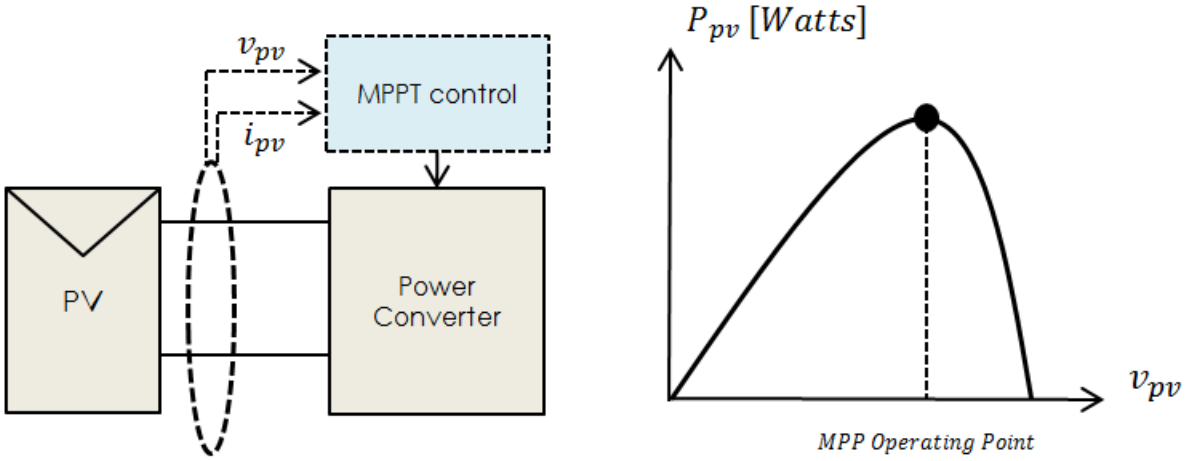

Figure 1.5: Maximum Power Point Tracking (MPPT) to harvest maximum energy from PV module

current is taken while in open circuit point $I_{pv} = 0$, maximum voltage is obtained. This issue is discussed in the following subsection.

1.4.2 Maximum Power Point Tracking

The operating point of the PV panels in PV power generation systems is determined by the power converter circuit connected to it. As it is mentioned earlier, the task of these power converter is to maximize power harvesting by using MPPT control algorithms as shown in Fig 1.5. As it can be seen, MPPT algorithm tries to control the operating point of the PV panel to harvest maximum input power ($i_{pv} \times v_{pv}$). PV panel's generated power in relation to it's operating voltage is demonstrated at Fig 1.5. As it can be seen, maximum power is obtained at a specific operating point. According to [6], the most famous algorithm used for MPPT is Perturbation and Observe (P & O), which works by perturbing the duty cycle of the power converter and therefore the voltage of the PV panel and observing its effect on the power curve [5].

1.4.3 Voltage Source Inverters

Beside maximizing energy harvesting from PV panels, the other important role of power converters is to synchronize the inverter with the grid. In two-stage single-phase micro-inverters, this task is performed by using Voltage Source Inverter (VSI) converter. In this thesis, a conventional H-bridge structure is used for implementing the voltage source inverter.

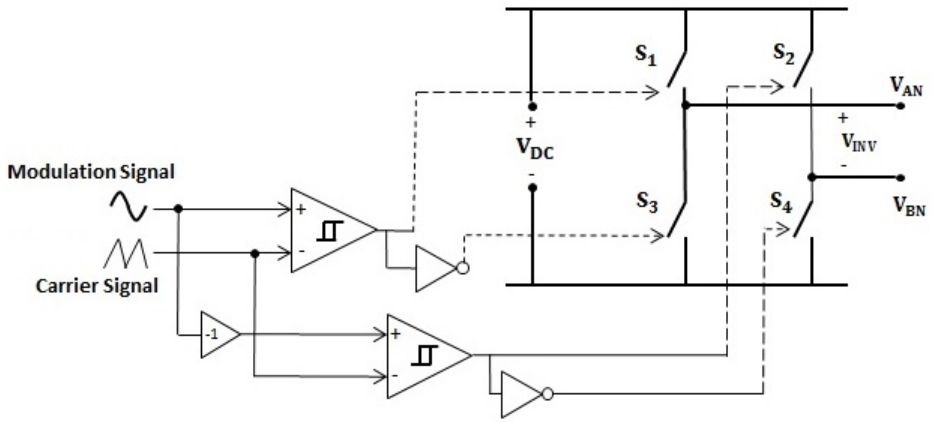

Figure 1.6: Full-bridge power converter with unipolar SPWM modulation scheme

H-bridge inverter circuit contain series and parallel combination of switches. Series combination of switches make a path which is referred to as a leg. Number of legs is dependent on whether the system is a three phase (uses 3 legs) or single phase (uses 2 legs). A single phase two-leg full-bridge inverter is shown in Fig 1.6. Input of inverter is a DC voltage which is obtained from the last stage of the power generation system. Output voltage of the inverter, is controlled by Pulse Width Modulation (PWM) technique. PWM creates an average output voltage by controlling the "ON/OFF duty cycle" of the switches used in the power converters. To create a sinusoidal signal in output of the inverter, unipolar sinusoidal-PWM (SPWM) modulation scheme is used. Modulation scheme controls inverter switches to produce a desired PWM output. As shown in Fig 1.6, unipolar SPWM modulation has two input signals described as follows

- *Modulation signal*: An low frequency AC signal with a specific frequency and maximum amplitude of one. This signal is used as reference signal to be generated at the output of inverter.
- *Carrier signal*: A high frequency triangular signal. This signal is compared to modulation signal in order to generate PWM switching command.

The unipolar SPWM modulation works by comparing carrier signal with modulation signal to determine which switch should be ON/OFF. As it can be seen in Fig. 1.6, two lower switches S3, S4, and two upper switches are commanded inversely by the modulation scheme in order to avoid short circuit.

Mechanism of SPWM switching is determined in Fig 1.7. Pulses which control S1, S2 switches are generated by the logic circuit of Fig 1.6. Combination of four switches is creating the inverter output voltage in form of high frequency pulses. As it is shown in Fig 1.7, inverter output can only have one of three values of V_{dc}, 0 , $-V_{dc}$ where V_{dc} is the input DC voltage.

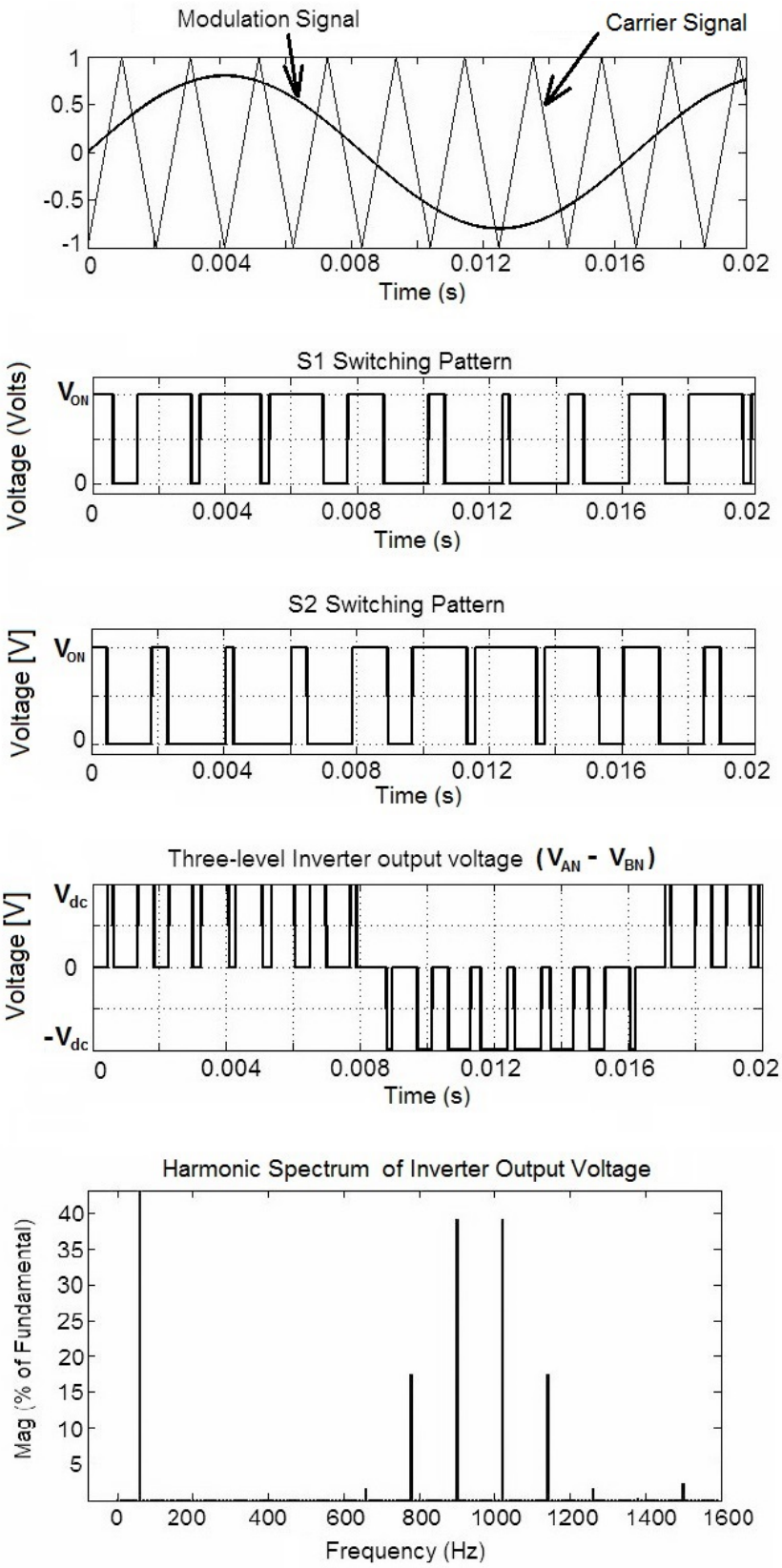

Figure 1.7: Unipolar SPWM modulation switching scheme

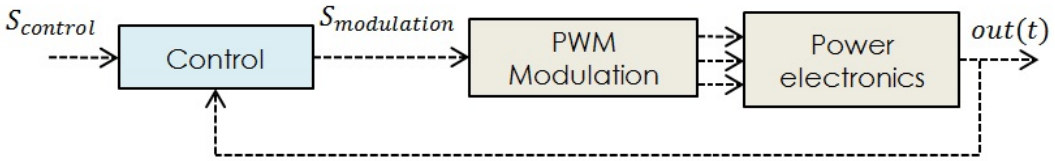

Figure 1.8: Basic diagram for controlling the output of power generation system

As it can be seen from Fig. 1.7, inverter output voltage contains a low frequency component and additional high frequency components. Average value of the inverter's output is a sinusoidal signal with the same frequency as the modulation signal. Harmonic spectrum of the inverter output is also demonstrated in Fig 1.7. Amplitude of output average sine signal can be described as follows

$$A_{inv} = V_{dc} A_{modulation} \tag{1.5}$$

where A_{inv} is amplitude of average output voltage and $A_{modulation}$ is the amplitude of the modulation signal and V_{dc} is input DC voltage to the inverter.

In (1.5), if amplitude of the modulation signal $A_{modulation}$ is maximum, which is one, average sine at inverter's output has maximum amplitude which is equal to input DC voltage. The amplitude of the modulation signal can be chosen to control the output of the inverter as follows

$$A_{modulation} = \frac{v*}{V_{dc}} \tag{1.6}$$

where $v*$ is desired value for the output voltage ranging from 0 to V_{dc}.

Basic concept of controlling the inverter's output is demonstrated in Fig 1.8. As it can be seen, a desired value $S_{control}$ is given to the controller to create a modulation signal $S_{modulation}$ in order to produce desired output signal. Controller is designed to control a certain output signal and is usually implemented using digital micro-electronics. The controller can be modeled by differential equations in time domain or it can be described by a transfer function in s-domain.

In micro-inverters usually a feedback control loop is designed to synchronize the inverter with utility grid. Detailed structure of the control system is going to be discussed in the following chapters.

Chapter 2

Adaptive Synchronization and Control

In this chapter, synchronization and control of a single-phase grid-connected inverter is discussed.

To utilize a proper control scheme for single-phase inverters, the role of the power converter in relation to the grid should be defined. Power converters in a micro-grid can be classified into different types depending on their operation. According to [11], power converters can be classified as follows

1. *Grid-forming power converters*: They can be represented as AC voltage sources, setting the voltage and frequency of a local grid.

2. *Grid-feeding power converters*: They are represented as AC current sources connected to the grid in parallel, designed mainly to deliver power to a energized grid. In this application, current source should be synchronized with grid voltage in order to regulate active/reactive power exchanged with the grid.

Grid-feeding power converters, need a generator or power converter to form the grid voltage to be able to operate. On the other hand, the grid-forming converters can operate independently with local loads since in the main grid, the voltage is produced by synchronous generators [11].

Grid-feeding power converters are suitable to be operated in parallel with other grid-feeding converters. Most of the distributed generation systems such as PV or wind is operating as grid-feeding [11]. Meaning, they are modeled as current sources injecting power to a pre-formed grid with pre-determined grid voltage.

To better determine how a Voltage Source Inverter injected power to a grid, a single-phase grid-connected inverter is modeled as shown in Fig. 2.1a. As discussed in the last chapter, the output of the inverter is a PWM voltage signal which is controlled by input the modulation signal to the inverter.

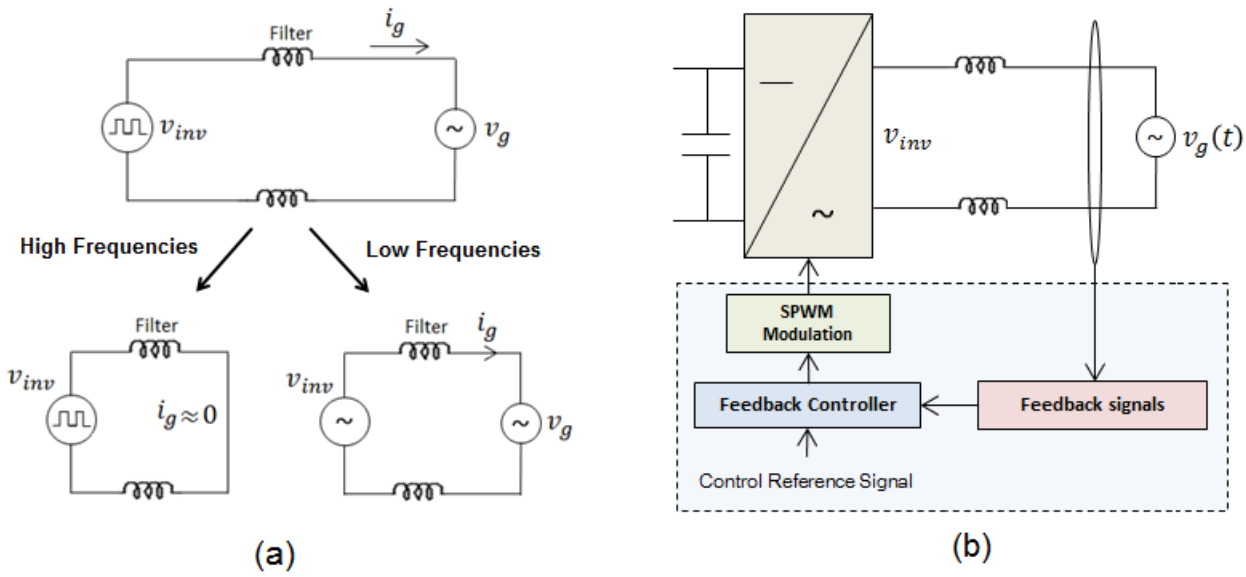

Figure 2.1: (a) Model of voltage source inverter connnected to the grid (b) General feedback control scheme grid-connected inverter

For grid-feeding converters, the idea is to input a modulation signal to the inverter such that the produced inverter voltage (v_{inv}) inject a sinusoidal current (i_g) into the grid. Supposing the inverter voltage is defined as below

$$v_{inv} = A_m sin(w_m t) + f(w_m, w_c) \tag{2.1}$$

where w_m is frequency of the modulation signal and w_c is the frequency of the carrier signal.

In (2.1), the inverter voltage contains high frequency PWM components and also low frequency modulation signal. The produced current (i_g) by the inverter voltage only contains low frequency components, since high frequency PWM signals are filtered by the inductance filters connecting the inverter to the grid as shown in Fig. 2.1a. But low frequency components of the v_{inv} is responsible for creating the output current.

This generated output current, should be in the same phase and frequency as the grid voltage at all times in order to deliver maximum average power to the grid. To create the output current, feedback control schemes are usually employed as shown in Fig. 2.1b. The control system, models the power electronic inverter of the Fig. 2.1 as a dynamic system in state-space representation, then control system tries to change the value of the feedback signals by comparing them to a desired reference signal and changing the inverter voltage value accordingly.

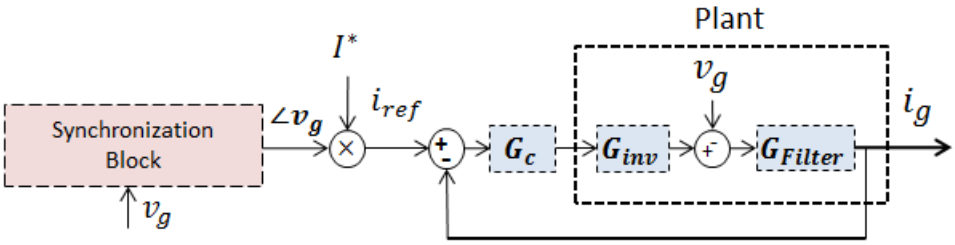

Figure 2.2: Block diagram of inverter current control scheme

2.1 Review of Current Control Schemes

To inject the current to the grid, several control schemes can be designed based on controlling the output current (i_g) to the grid via a feedback loop.

The block diagram of a conventional feedback current control system is shown in Fig. 2.2. As demonstrated in the figure, the current controller transfer function is modeled by G_c, also the inverter and the output filters are modeled by the transfer function as G_{inv} and G_{filter}.

To control the output signal, first a reference sinusoidal is created which has the same phase as the grid voltage to deliver the maximum power. The controller objective is to force the output current i_g to track the reference current i_{ref}.

The closed-loop transfer function of the current control system can be expressed in s-domain as follows

$$\begin{aligned} I_g(s) &= (I_{ref} - I_g)G_cG_{inv}G_{filter} \\ (1 + G_cG_{inv}G_{filter})I_g(s) &= I_{ref}(s)G_cG_{inv}G_{filter} \end{aligned} \tag{2.2}$$

therefore

$$\frac{I_g(s)}{I_{ref}(s)} = \frac{G_{loop}}{1 + G_{loop}} \tag{2.3}$$

$$G_{loop} = G_c(s) \times G_{inv}(s) \times G_{filter}(s) \tag{2.4}$$

To accurately track the reference signal, the transfer function of the current controller ($G_c(s)$) should be able to make the transfer function of (2.3) equal to one at the frequency of the grid as follows

$$\frac{I_g(jw_g)}{I_{ref}(jw_g)} = \frac{G_{loop}}{1 + G_{loop}} \approx 1 \tag{2.5}$$

where w_g is grid voltage.

For (2.5) to be equal to one, the current controller at the fundamental frequency of the grid should be defined as follows

$$G_c(jw_g) \approx \infty \tag{2.6}$$

Equation (2.6) means that the current controller should provide very high gain at the frequency of the grid to be able to track the reference current and regulate the output current.

The simple Proportional-Integral (PI) controller which is used in variety of application, is defined as follows

$$G_{PI} = K_p + \frac{K_i}{s} \tag{2.7}$$

where K_p is the proportional gain and K_i is the gain of the integral part.

The PI controllers have infinite gain at DC due to its integral part, thus it can track DC signals accurately. Proportional gain can be adjusted to increase the speed of the convergence. Furthermore, a derivative part can be added to PI controller to reduce overshoot and help the transient response.

Since the gain of PI controllers is not very high at AC frequencies it will create a steady-state error in tracking AC signals. If the PI controller defined in (2.7) is used as the current controller, the output current cannot track the the reference signal accurately and phase and amplitude of the output current will be different than the reference current i_{ref}. This is due to the fact that the PI controller can not provide very high gain at frequency of the grid unless the bandwidth of the controller is chosen wide enough to provide a high gain at the frequency of interest. A very wide bandwidth PI controller can not practically be used due to a very small sampling time it will require. Also a very wide bandwidth PI controller will make the output current vulnerable to the grid harmonic distortions [13].

For three-phase systems defined in Synchronous Reference Framework (SRF), PI controllers can be used since the SRF will transform the 3-phase AC signals to DC values. However this will require use of additional frame transformations which in turn creates complexity and computational burden to the system [12].

To overcome the problems stated in Tracking AC current signal in a single-phase grid-connected inverters, Proportional-Resonant (PR) controllers have been used instead of the PI controller in the literature. The transfer function of the PR controllers is expressed as follows

$$G_{PR} = K_p + \frac{K_i s}{s^2 + w_0^2} \tag{2.8}$$

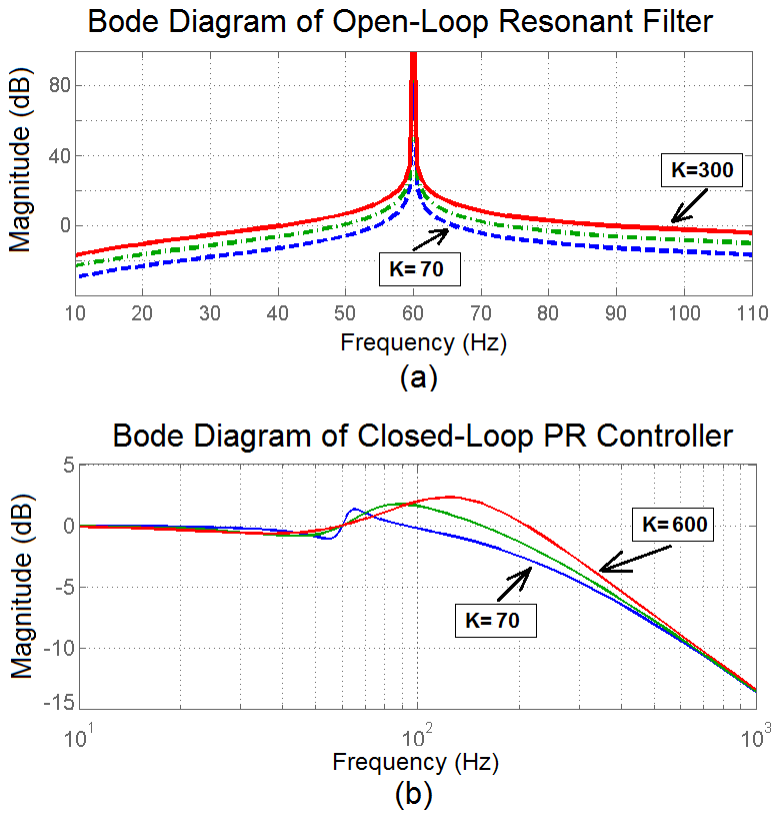

Figure 2.3: Bode diagrams of (a) Open-loop resonant filter (b) Closed-loop PR current controller

where K_p is the simple proportional gain like the one in PI controller, K_i is the gain of the resonant filter and w_0 is the resonant frequency of the resonant filter.

The bode diagram of the resonant controller and the closed-loop bode diagram of the current controller shown in Fig. 2.2 is demonstrated in Fig. 2.3. As it can be seen from Fig. 2.3a, the resonant filter is frequency selective and will only provide a very high gain at the selected resonant frequency w_0. In comparison with PI controller, the PR controller has a high gain over an AC frequency instead of DC. This high gain at the resonant frequency, will make the closed-loop transfer function described in (2.5) equal to unity and thus force the output current (i_g) follow the input reference signal (i_{ref}). The resonant gain of PR controller (K_i) in (2.8) affects the closed-loop bandwidth of the current controller as shown in bode diagram of Fig. 2.3b and also frequency selectivity of the resonant filter as shown in Fig. 2.3a. High values of the resonant gain (K_i) will make the current controller dynamic performance quite fast. However, at the same time, the high values of the mentioned parameter, will reduce the frequency selectivity of the PR controller and makes it vulnerable to the harmonic distortions that might be presented in the (i_{ref}) signal due to the distortions that might be presented in the grid voltage. This issue will be discussed further into details

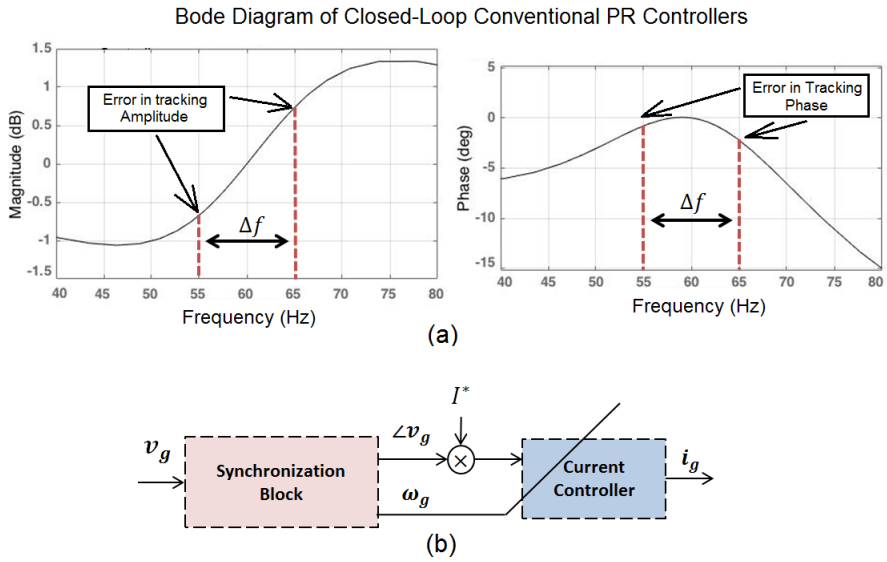

Figure 2.4: (a) Bode diagrams of a closed-loop PR controller during grid frequency variations (b) Adaptive current controller

in Chapter III of this thesis. High values of the resonant gain might create stability problems since operating at the stability margins will make the control parameters more sensitive to noises.

2.2 PR Tracking Problem: Grid Frequency Fluctuations

The accurate tracking of AC reference signal by the PR controller can also be explained via the Internal Model Principle. Based on the Internal Model Principle (IMP), perfect tracking (or complete rejection) of input reference signal can be achieved only if the system satisfies the following conditions:

1. Closed-loop system is asymptotically stable.
2. Mathematical model of the reference signal is included in the open-loop transfer function.

The PR controller utilizes the IMP to achieve perfect tracking by including s-transform of a sinusoidal signal into its transfer function as shown in (2.8).

As shown in Fig. 2.2, the reference current is created by the synchronization block in order to have the same phase as the grid voltage. And if grid operates at its nominal frequency, according to IMP principle, a PR controller with the its resonant frequency tuned at the nominal frequency of the grid is able to track track the reference signal accurately.

If the grid frequency fluctuates away from its nominal value (which is used as resonant frequency (w_0) of PR controller), the current controller would fails to track the reference

signal. Any fluctuations in the grid frequency would result in reduced accuracy in amplitude and phase of the output current. Therefore, internal model of PR controller must be adjusted to grid frequency variations.

The effect of frequency variations of the grid on tracking ability of PR controller is shown in Fig. 2.4a. For instance, higher frequencies would decrease the power factor and increase the amplitude, while lower frequencies would attenuate the amplitude.

To solve this issue, one way is to increase the bandwidth of the PR controller. Larger bandwidth will make the current controller less sensitive to grid frequency changes but it also makes the controller more vulnerable to the grid harmonic distortions.

Other solution which does not require changing the bandwidth of the resonant controller is to adapt the resonant frequency of PR controller to frequency variations by feeding the grid frequency to the controller.

The estimated frequency of the grid is not only required for making the current controller adaptive but is also required for real-time monitoring of the grid. IEEE 1547 and other regulatory standards, require the power generation systems to cease powering the grid if the grid frequency is above/below a pre-determined threshold. In this thesis, the frequency of the grid is estimated by the synchronization algorithm as shown in Fig. 2.4b. The proposed synchronization block is introduced in the next section.

2.3 Synchronization of Adaptive PR Controllers

One of the most famous synchronization methods mentioned in literature is Synchronous-Reference-Frame Phase-Locked-Loop (SRF-PLL) which is commonly used for three-phase systems. A PLL consist of a Phase Detector (PD), Loop Filters (LF) and a Voltage Controlled Oscillator (VCO) as shown in Fig. 2.5b. The block diagram of the SRF-PLL used for single-phase systems is shown in Fig. 2.5b. As it can be seen, in single-phase SRF-PLL the delayed version of the input signal is used for creating phase detection.

However, this system does not perform well under grid frequency variations and creates oscillatory distortions on top of the estimated frequency. It is due to the fact that grid frequency is considered to be fixed when the delayed version of the input signal is created in the Phase Detector block. This problem also exists in the phase-shift structure used in Multiharmonic Decoupling Cell-PLL (MHDC-PLL). Other single-phase PLL is enhanced-PLL (EPLL) which uses an adaptive nonlinear filter as its Phase Detector block. The EPLL dynamics is slow and not suitable when the fast response is an issue [29]. Fast response of synchronization block is an important issue, since power systems should act in response to abnormal frequencies in a specific time-frame as it is mentioned in IEEE 1547. The performance of the previously proposed methods are evaluated in literature [29].

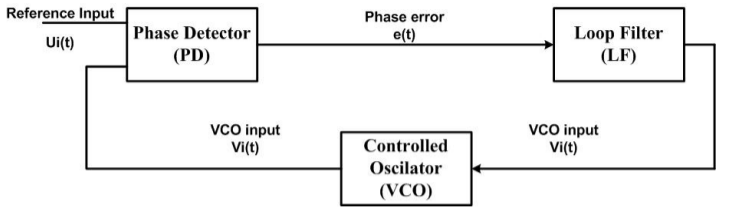

(a) © IEEE 2011

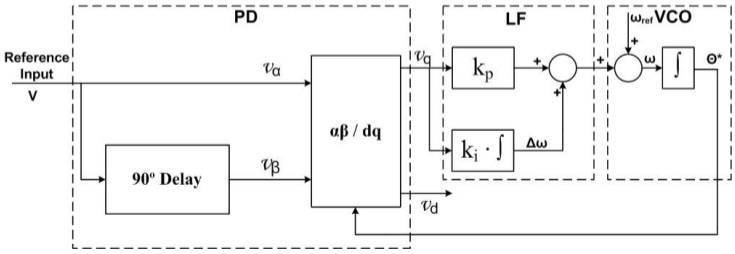

(b) © IEEE 2011

Figure 2.5: Block diagram of (a) General structure of PLL (b) Single-phase SRF-PLL (images-source: [46] Copyright ©2011, IEEE)

Zero-crossing method is another alternative synchronization method to PLLs. However, the frequency in this method is only calculated twice in each cycle which leads to poor frequency detection and monitoring specially if the grid frequency varies [30].

Another alternative synchronization method is Frequency Locked Loop (FLL), which unlike the PLL, creates a feedback loop to control the estimated frequency of the grid rather than its phase. Since the grid frequency is more stable than its phase, this method provides more stability and less sensitivity to the changes in the phase of the grid.

In the following sections of this chapter, a novel FLL is going to be proposed which has the following characteristics:

1. Synchronization is based on Frequency Locked Loop.

2. Frequency selective filters in FLL and PR current control makes the output current partially immune to high order grid harmonic disturbances.

3. Fast frequency estimation and phase synchronization is achieved while meeting the IEEE 1547 frequency disturbance constraints.

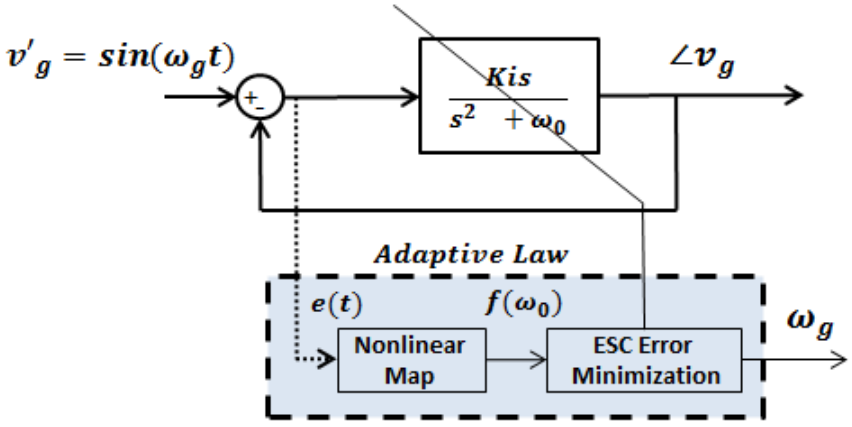

Figure 2.6: Block diagram of proposed ESC-FLL synchronization method

2.4 Proposed ESC-FLL Synchronization Block

As mentioned in previous sections, synchronization block should be able to provide phase and frequency information of the grid for proper synchronization of the output current with the grid voltage.

The block diagram of the proposed synchronization method is shown in Fig. 2.6 where v'_g is the normalized value of the grid voltage. In the proposed method, a resonant filter based on internal model principle is placed in a feedback loop to provide the phase information of the grid.

If the frequency of the grid changes, the phase error between the grid voltage and output of the filter is expressed as follows

$$\theta_e = tg^{-1}\left[\frac{(w_g^2 - w_0^2)}{(K_i w_g)^2}\right] \tag{2.9}$$

where w_g is the frequency of the grid and w_0 is the resonant frequency of the filter in the proposed synchronization block.

To make remove the phase-error in (2.9), an adaptive algorithm is proposed as shown in Fig. 2.6. The adaptive algorithm is divided into two parts:

1. Nonlinear Map: Deriving an equation which maps the error signal in the proposed feedback loop to the frequency difference.

2. Extermum Seeking: Forcing the system to operate at the grid frequency.

The objective is to minimize the phase error in (2.8) to zero so the new value of grid frequency is estimated. Detailed analysis of this process is subsequently demonstrated in the following.

2.4.1 Nonlinear Map Based on Error Amplitude

The transfer function of a resonant filter is given by

$$G_R(s) = \frac{K_i s}{s^2 + w_0^2} \tag{2.10}$$

Therefore the closed-loop system is as follows

$$G_{loop} = \frac{I_{ref}}{V'_{grid}} = \frac{G_R(s)}{1 + G_R(s)} \tag{2.11}$$

where V'_{grid} is the normalized grid voltage.

The error signal of the closed-loop resonant filter can be expressed as follows

$$E(s) = \frac{1}{1 + G_R(s)} V'_g(s) \tag{2.12}$$

Considering (2.10), the error signal is expressed as

$$E(s) = \frac{s^2 + w_0^2}{K_i s + s^2 + w_0^2} V'_g(s) \tag{2.13}$$

Equation (2.13) expresses the closed-loop error of the system in Fig. 2.6. If the frequency of the grid is equal to the resonant frequency (i.e., $s = jw_0$), then G_R is infinite and the error signal is zero and perfect tracking is achieved. However, if the frequency of the grid fluctuates and $s \neq jw_0$, an error signal is generated. By formatting the resonant filter as follows

$$G_R = \frac{1}{s^2 + w_0^2} \frac{N_0}{D_0} \tag{2.14}$$

The error signal at the specific grid frequency w_g can be expressed as follows

$$e(t) = A_e cos(w_g t + \theta) \tag{2.15}$$

$$A_e = \left| \frac{(s^2 + w_0^2) D_0(s)}{(s^2 + w_0^2) D_0(s) + N_0(s)} \right|_{s=jw_g} \tag{2.16}$$

where the amplitude of the error signal is denoted by A_e which contains information about grid frequency variation as follows

$$A_e \propto (w_0^2 - w_g^2) \tag{2.17}$$

If the error amplitude, A_e, is extracted and minimized (by tuning w_0), then the resonant frequency w_0 converges to w_g. The term A_e is extracted by utilizing

$$e^2(t) = \frac{1 + cos(2w_g t + 2\theta)}{2} A_e^2 \tag{2.18}$$

and passing it through a notch filter to remove the double frequency component, expressed as follows

$$G_{notch} = \frac{s^2 + w_n^2}{s^2 + w_n^2 + 2\xi w_n s} \tag{2.19}$$

where ξ is the damping factor and w_n resonant frequency of the notch filter which is a fixed value and is defined to be twice the nominal grid frequency $120Hz$.

In (2.19), the bandwidth of the notch filter is chosen to be wide enough in order to make the notch filter insensitive to the grid frequency changes and to remove the double frequency component of (2.18) during grid frequency changes. The result of passing the error in (2.19) through the notch filter in (2.18) would be

$$e(t)^2 \mid_{Notch} \approx \frac{1}{2} A_e^2 \tag{2.20}$$

Assuming that the resonant frequency w_0 is adjustable, it follows that (2.20) is a function of the resonant frequency as follows

$$f(w_0) = \frac{1}{2} A_e^2 \tag{2.21}$$

However, it should be noted that nonlinear map proposed in (2.21) is not always the function of frequency difference.

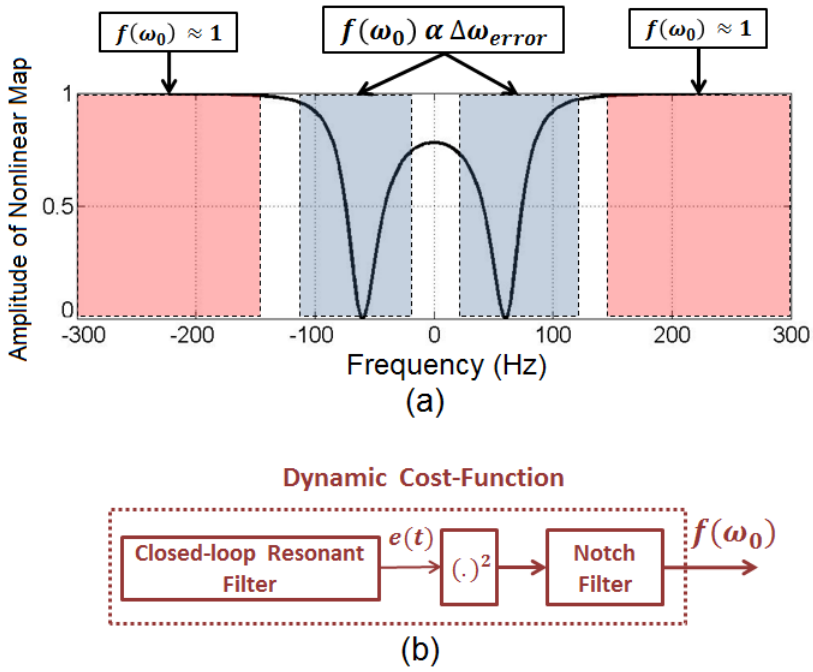

Figure 2.7: (a) Block diagram of proposed nonlinear map used in synchronization block (b) Method used to derive the nonlinear map

Plot of equation (2.21) as a function of resonant frequency is demonstrated at Fig. 2.7a. As it can be seen, this map has a minimum at the frequency of grid. Equation (2.21) is a nonlinear map with only one extremum value which is the grid's frequency w_g. Combining (2.17) and (2.21) we have

$$f(w_0) \propto (w_0^2 - w_g^2)^2 \tag{2.22}$$

which is approximated by a second-order Taylor's series expansion around w_g as follows

$$f(w_0)\big|_{w_0=w_g} \propto (w_0 - w_g)^2 \tag{2.23}$$

However this minimum value of the $f(w_0)$ is a local extremum not a global one. The frequency selectivity of this map is determined by the integral gain of the resonant filter used in the synchronization block at Fig. 2.6. If this gain is chosen to be too small, any frequency deviation forces the squared amplitude of error to be equal to unity which is outside of the area of the map with local minimum at grid frequency. Therefore, the frequency of the grid cannot be estimated in that situation.

The method used to derive this nonlinear map is shown in Fig. 2.7b. In the following, the perturbation extremum seeking is going to be introduced and used to find the extremum value of this nonlinear map which the grid frequency.

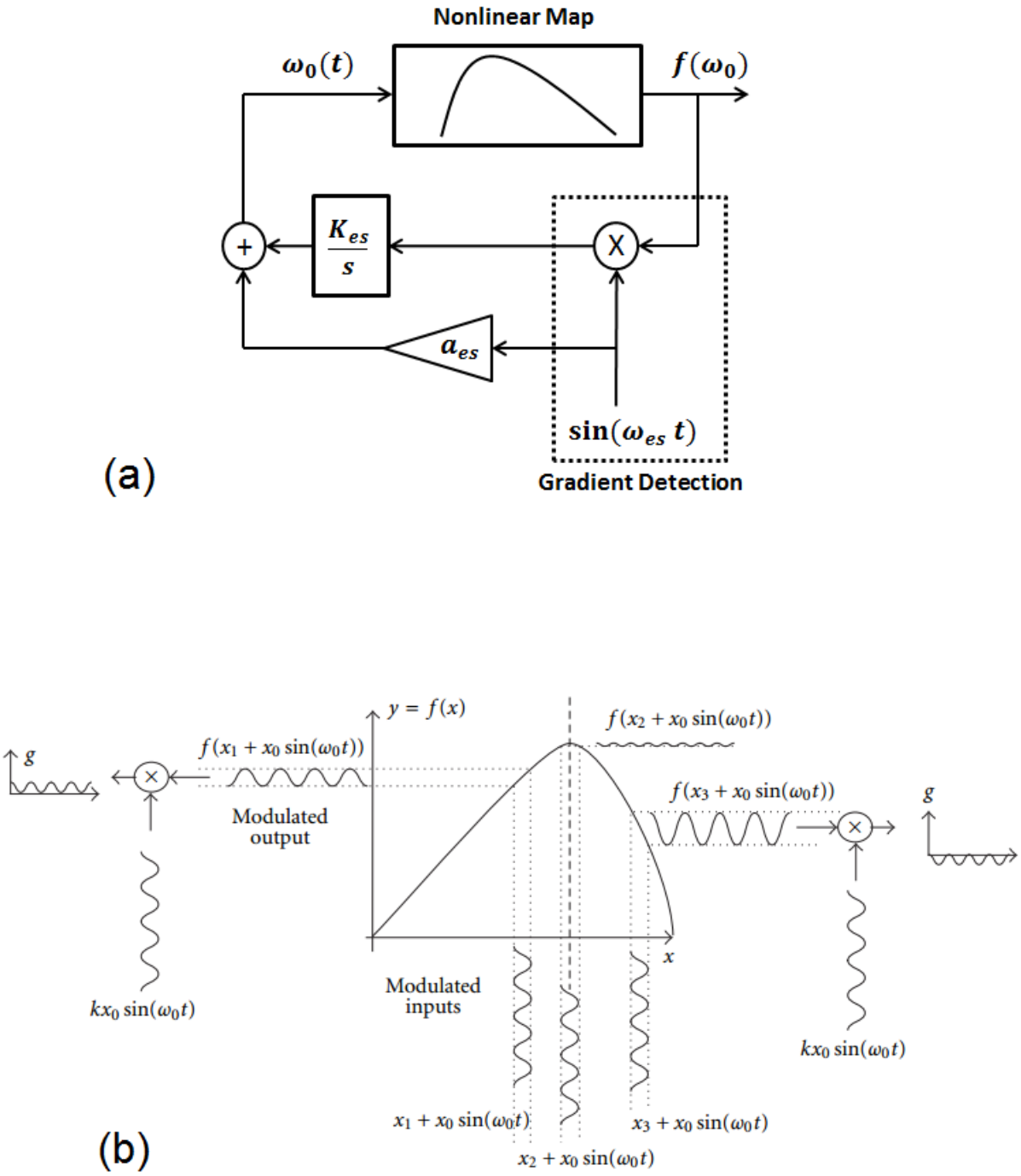

Figure 2.8: (a) The block diagram of perturbation extremum-seeking algorithm (b) The gradient detection method by perturbation extremum-seeking (image-source: [14] used under *Creative Commons Attribution License (CC BY 4.0)*)

2.4.2 Introduction to Perturbation Extremum Seeking

To minimize the nonlinear map of (2.21), perturbation extremum seeking is proposed. The general idea of the perturbation extremum seeking is shown in Fig. 2.8a.

Perturbation extremum seeking finds the extremum value of the nonlinear map by adding an perturbation signal to the input variable of the map as follows

$$\hat{w_0} = w_0(t) + a_{es}sin(w_{es}t) \tag{2.24}$$

Thus, the generated output of of the nonlinear map has the output as follows

$$f(\hat{w_0}) = f\Big(w_0(t) + a_{es}sin(w_{es}t)\Big) \tag{2.25}$$

If (2.25) is expanded and approximated by the first order Taylor's series, we have

$$f(\hat{w_0}) \approx f(w_0) + a_{es}sin(w_{es}t)\frac{df(w_0)}{dw_0} \tag{2.26}$$

Then the gradient of the nonlinear map at the current operating point is detected by multiplying the output of the nonlinear map by the same perturbation signal used at the input of the map. If (2.26) is multiplied by the perturbation signal, the output is expressed as follows

$$\begin{aligned} & f\Big(w_0 + a_{es}sin(w_{es}t)\Big)sin(w_{es}t) \\ & \approx f(w_0)sin(w_{es}t) + a_{es}sin(w_{es}t)^2\frac{df(w_0)}{dw_0} \\ & \approx \frac{a_{es}}{2}\frac{df(w_0)}{dw_0} + f(w_0)sin(w_{es}t) - \frac{a_{es}}{2}cos(2w_{es}t)\frac{df(w_0)}{dw_0} \end{aligned} \tag{2.27}$$

In (2.27), the first term is the gradient of the map with respect to the perturbed variable. The other terms are higher order AC signals related to the perturbation frequency (w_{es}).

After that, the extremum-seeking control determines a new value for the independent variable of the map (w_0) by proposing the dynamic law expressed as

$$\dot{w_0}(t) = -K_{es}\left[\frac{a_{es}}{2}\frac{\partial f(w_0)}{\partial w_0} + f(w_0)sin(w_{es}t) - \frac{a_{es}}{2}cos(2w_{es}t)\frac{\partial f(w_0)}{\partial w_0}\right] \tag{2.28}$$

Higher frequency perturbation terms in (2.28) are going to be eliminated by the integrator estimating the independent variable. Thus, dynamics of the estimated frequency is only affected by the gradient of the map and (2.28) can be approximately by

$$\dot{w_0}(t) \approx -K_{es}\frac{a_{es}}{2}\frac{\partial f(w_0)}{\partial w_0}\bigg|_{w_0 = operating-point} \tag{2.29}$$

As already represented in (2.23), the gradient of the nonlinear map in the proposed synchronization block, can be expressed as a second order polynomial equation with minimum around the grid frequency w_g. Thus, (2.28) can be expressed as

$$\dot{w_0} \propto -\frac{K_{es}a_{es}}{2}\frac{\partial}{\partial w_0}\Big[(w_0 - w_g)^2\Big]\Big|_{w_0=operating-point} \tag{2.30}$$

As it can be seen in (2.30), if the value of the resonant frequency w_0 is smaller than the grid frequency w_g, the gradient of the second order polynomial is negative and if this value is multiplied by the gain of the extremum-seeking, thus overall a positive value will be achieved. Meaning, if the value of the resonant frequency is smaller than the extremum-value it will be increased and if the value of the resonant frequency is bigger than the extremum value, it will be decreased. When the system reaches the value of the extremum, the gradient of the system is equal to zero, thus the system will stay at this value as it is demonstrated in Fig. 2.8b.

If the proposed map has minimum extremum like in the case of the proposed map in Fig. 2.7, the gain of the extremum-seeking (K_{es}) is chosen to be negative and if the system has maximum value, this gain is chosen to be positive in order for the independent variable reaches the minimum/maximum point. This rule can be stated as follows

$$sign[K_{es}] = -sign[\frac{\partial^2 f}{\partial w_0^2}] \tag{2.31}$$

Designing and selecting ES parameters affects the system's transient and stability characteristics. In particular, large values of a_{es} (amplitude of perturbation) and K_{es} (extermum-seeking gain) result in faster convergence but also increase the sensitivity to disturbances.

The nonlinear maps which is used in extremum-seeking control, can be a static map, which is a input/output function or it can be a dynamic map meaning the map is derived from a dynamic system. It should be noted that, if a dynamic map is used in extremum-seeking control, its transient dynamics should be fast enough, so that the extremum-seeking control can treat this dynamic system as a static map. The proposed synchronization block in this thesis (ES-FLL) is a dynamic system. It should be noted that, the transient dynamics of the resonant feedback loop in Fig. 2.6 should be faster than the extremum-seeking controller used to estimate the grid frequency.

2.4.3 Proposed Frequency Estimation via Extremum Seeking

The proposed extremum-seeking control method to determine the grid frequency is shown in Fig. 2.9. As it can be seen from the diagram the squared amplitude of the error signal is first derived from the closed-loop resonant filter via a notch filter. This will create a

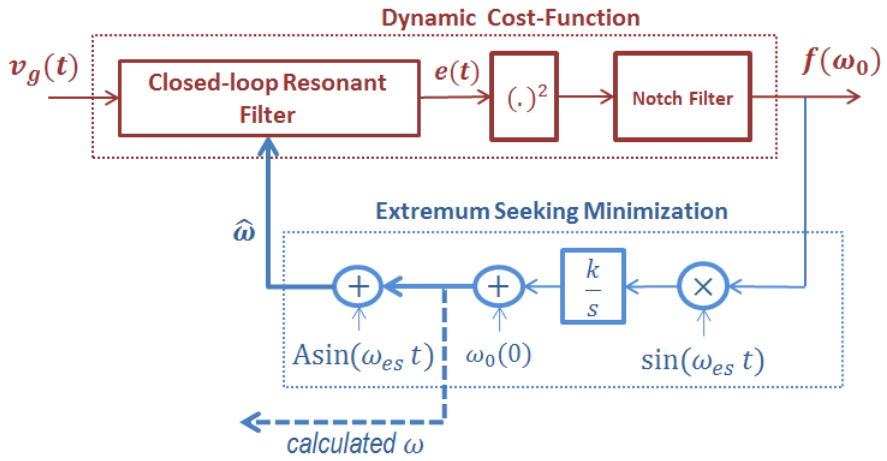

Figure 2.9: The block diagram of the proposed extremum-seeking algorithm to estimate the grid frequency

dynamic map which is already shown in Fig. 2.7a. Then perturbation extremum-seeking is used to estimate the frequency of the grid by seeking the minimum point of the map.

If the grid frequency has variations, then the error in the feedback loop is created and the minimum value of this map is also varied which will make the extremum-seeking to estimate a new value.

The reason, a notch filter is used to remove the double frequency component of the squared error signal instead of a Low Pass Filter (LPF) can be explained based on the extremum-seeking system in Fig. 2.9. As discussed previously, the dynamic map has perturbing component related to the frequency to perturbation (w_{es}) which should not be removed during the extraction of the map from the error signal. The value of the w_{es} is chosen to be around 500Hz which is high enough to not be removed by the notch filter. The resonant frequency of the notch filter is fixed around 120Hz (twice the nominal frequency of the grid 60Hz). Since the notch filter is used in the frequency estimation loop, its resonant frequency can not be adapted to grid frequency changes. However, as already mentioned, the bandwidth of the notch filter is chosen to be wide enough to attenuate the variations of the grid frequency.

2.5 Voltage Control Loop: DC-link Regulation

In the current control block diagram of Fig. 2.2 it was assumed that the amplitude of the reference current I^* is a constant value. This value determines the amount of the amplitude of the output current and thus the amount of the energy to be delivered to the grid.

As it was discussed in the last chapter, the inverter is responsible for converting the input DC value to the output inverter voltage v_{inv}. For delivering current to the grid, the

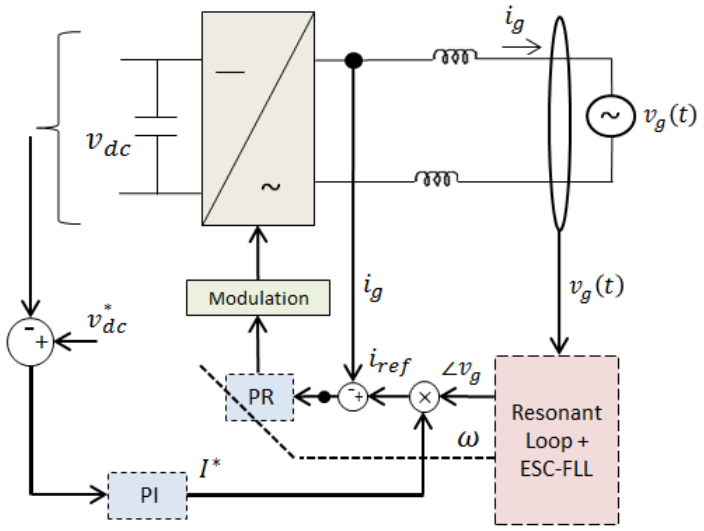

Figure 2.10: The block diagram of the proposed outer voltage control loop

AC signal in the output of the inverter as shown in Fig. 2.1a, should have a large amplitude than the grid voltage v_g in order to be able to inject current into the grid. Therefore, DC-link voltage V_{DC} at the input of the inverter is the maximum amplitude the inverter voltage v_{inv} can take. The detailed analysis of the DC-link dynamics is presented in literature [54]-[56].

To regulate the value of the DC-link voltage (V_{DC}), an outer voltage loop is demonstrated at Fig. 2.10. As it can be seen, the PI controller is regulating the DC-link voltage by controlling the amplitude of the reference current (I^*). Since the variable to be regulated is a DC signal (V_{DC}), thus the PI controller is used to regulate the DC-link voltage and determine the amplitude of the reference current for the PR current control loop.

2.5.1 Eliminating Double Frequency Ripple by Adaptive Notch Filter

The DC-link voltage is not a pure DC signal and contains ripples with frequency twice the frequency of the grid expressed as follows

$$v_{dc}(t) = V_{DC} + A_{dc}sin(2w_g t) \tag{2.32}$$

The reason for such a ripple is in fact the nonlinear nature of PWM modulation used to generate the inverter voltage.

According to [56] [54], the switching function of the inverter, relating the input/output signals in the inverter can be expressed accurately by the double Fourier series as follows

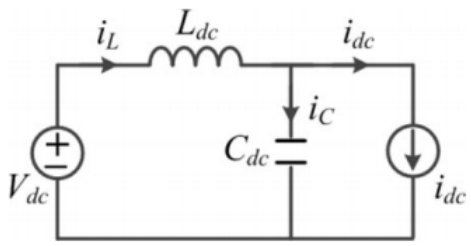

Figure 2.11: The equivalent model of DC-link circuit (image-source:[55] Copyright ©2015, IEEE)

$$s(t) = Mcos(w_g t) + \frac{2}{\pi}\sum_{m=1}^{+\infty}\sum_{n=-\infty}^{+\infty}\frac{1}{m}J_{2n-1}(m\pi M)cos[(m+n-1)\pi]cos[2mw_c t + (2n-1)w_g t] \tag{2.33}$$

where J is the Bessel function, M is the modulation ratio, m and n are integers. w_c is the frequency of the modulation carrier and w_g is the frequency of the modulation signal which is the same as the fundamental frequency of the grid.

The relationship between the input current to the inverter and the injected current can be expressed as follows

$$\begin{aligned} i_{dc}(t) &= s(t)i_{out}(t) \\ i_{out} &= Isin(w_g t) \end{aligned} \tag{2.34}$$

where $s(t)$ is the switching function defined in (2.33). Replacing $s(t)$ from (2.33) into (2.34) results in

$$i_{dc}(t) = I_{dc} + I_1 sin(2w_0 t) + i_{hf}(t) \tag{2.35}$$

As it can be seen from (2.35), the input current into the inverter consists of a dc value (I_{dc}), a double frequency component and a high switching frequency component (i_{hf}). Therefore, inverter can be modeled by a current source as shown in Fig. 2.11 [56] [54].

In the equivalent circuit of the DC-link at Fig. 2.11, the DC-link voltage is determined by two sources. The double frequency component in the modeled current source of (2.35), will affect DC-link voltage according to principle of superposition.

This double frequency ripple on top of the DC-link voltage is undesired since it will enter the control loop and will reduce the quality of the output current by creating a third harmonic component in the reference current in the PR current control loop. The

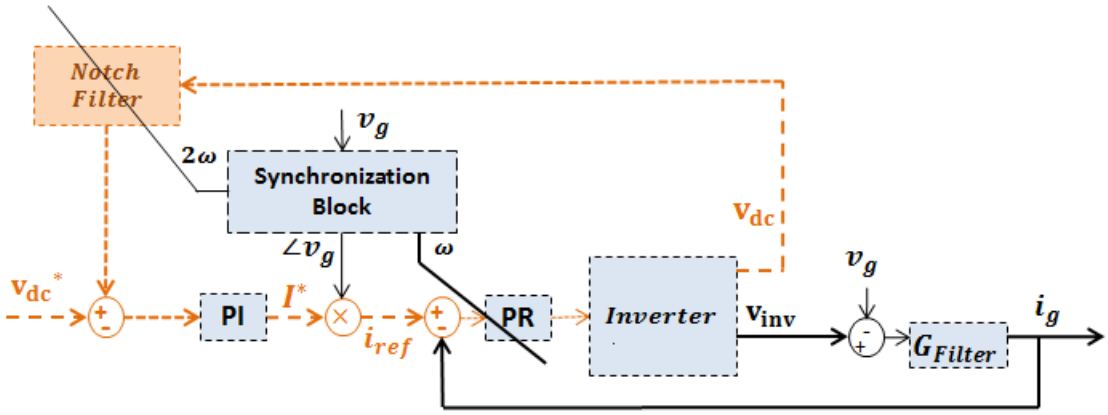

Figure 2.12: The block diagram of the voltage control loop with proposed adaptive notch filter

quality of the output current is important since according to the grid-tied standards such as IEEE 1547, the THD of the injected current to the grid should be below a pre-determined threshold as already discussed in the previous chapter.

Choosing larger decoupling capacitors at the DC-link will help attenuating the undesired double frequency component. The value of the DC-link capacitor can be chosen according to the maximum tolerable ripple on the DC-link by the formula expressed as below [59]

$$C_{dc} = \frac{P_{dc}}{w_g \times V_{dc} \times \Delta V_{ripple}} \tag{2.36}$$

where P_{dc} is rated power from PV panel, V_{dc} is average DC-link voltage and ΔV_{ripple} is the maximum tolerable ripple.

To remove the double frequency ripples effectively, one way is to reduce the bandwidth of the PI voltage controller. However this will reduce the transient performance of the DC-link. Since, in renewable energy systems, the power can change abruptly which require the voltage controller to converge quickly. Another solution have been proposed in [58] is to estimate the DC-link ripple which will increase the computational burden for implementing the controller via Micro-controller.

In this thesis, to remove the double frequency ripple, an adaptive notch filter is proposed as shown in Fig. 2.12. As it can be seen, first the double frequency component of the voltage is removed by the filter and then the remaining DC component is regulated in the voltage control loop. The resonant frequency of the notch filter is adapted by twice the estimated frequency by the proposed synchronization block. Adapting the frequency of the grid will make sure the double frequency ripple is attenuated effectively during grid

frequency variations since this double frequency ripple is always equal to the twice the value of the grid voltage.

Chapter 3

The Effect of Grid Distortion

In this chapter, the effect of grid harmonic distortions on the proposed synchronization block and adaptive PR current controller is going to be discussed and analyzed.

The harmonics presented in the grid can affect the performance of the proposed synchronization and control schemes and effectively increase the THD of the output current above the thresholds set by IEEE 1547 standard.

Harmonic distortions in the grid voltage can happen due to different reasons such as non-linear loads and increased power electronics.

The effect of grid harmonic distortion on the proposed grid-connected control system (of the previous chapter) is going to analyzed in two separate parts expressed as below

1. Synchronization block (ES-FLL)

2. Current control scheme (PR Controller)

In synchronization task, the voltage harmonics affects the phase/frequency estimation of the grid and depending on the structure of the controller, it may create unwanted components [20], [24]. Therefore, the output current is affected and may contain harmonic distortion.

Synchronization methods such as Second Order Generalized Integrator PLL (SOGI-PLL), Inverse Park Trasform PLL (IPT-PLL), Synchronous Reference Frame PLL (SRF-PLL) and Double Synchronous Reference PLL (DSRF-PLL) provide partial immunity to the high frequency grid distortions due to their frequency selectivity (such as second order schemes) [42], [43], [44], [45], [29]. To attenuate the lower order grid harmonics, one option is to limit the bandwidth of the synchronization controller [47], [43]. However, a sufficiently narrow bandwidth control scheme (that attenuates harmonics) slows the speed of synchronization [43], [24]. The synchronization speed is of prime importance since grid-tied standards require the micro-girds to cease powering the grid during abnormal conditions such as frequency variations.

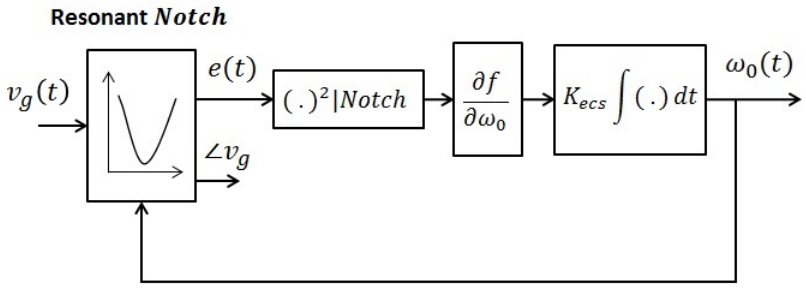

Figure 3.1: Block diagram of frequency estimation loop

Synchronization structures such as Enhanced PLL (EPLL) or T/4 Delay PLL do not respond well to the high harmonic distortions [29]. The harmonic rejection method proposed in [48], eliminates grid harmonic distortions. However, the effect of grid frequency variations is not studied in [48]. The NTD-PLL introduced in [49] is only immune to distortions at the nominal grid frequency. As stated in [49], ETD-PLL can adapt to grid frequency variations. However, according to [42], this method does not entirely eliminate harmonics. Nevertheless in all aforementioned cases, the important factor for synchronization is the ability to adhere to the interconnected standards.

Other than grid synchronization, another issue requiring attention in a polluted grid, is how much the produced current harmonics are affected by the harmonics presented in the grid voltage. In general, conventional PR controllers with a infinite gain at resonant frequency are not well-equipped to deal with this problem as demonstrated in [50]-[52].

In this chapter, the effect of grid distortions on synchronization block is analyzed, then the structure of the proposed FLL is modified to withstand grid distortions and provide accurate estimation of grid frequency and phase. The effect of distortion on PR current control system is also analyzed and its structure is enhanced to be able to regulate the output current more accurately during the grid harmonic distortions.

3.1 The Effect of Distorted Grid on Synchronization Block

The proposed frequency estimation loop is shown in Fig. 3.1. As it can be seen, the relationship between the input grid voltage $v_g(t)$ and error of the closed-loop resonant filter $e(t)$ can be expressed as a notch filter as follows

$$\frac{E(s)}{V_g(s)} = \frac{1}{G_{Resonant}+1} = \frac{s^2+w_0^2}{s^2+w_0^2+K_i s} \tag{3.1}$$

where $G_{Resonant}$ is the resonant filter and w_0 is its resonant frequency and K_i is representing its resonant gain.

To determine how grid harmonic distortions affect the extremum seeking frequency estimation, let us suppose that the grid voltage v_g contains second and third harmonics as follows

$$v_g(t) = A_g sin(w_g t) + v_{h2}(t) + v_{h3}(t) \tag{3.2}$$

where

$$\begin{aligned} v_{h2}(t) &= A_{h2} sin(2w_g t) \\ v_{h3}(t) &= A_{h3} sin(3w_g t) \end{aligned} \tag{3.3}$$

are the second and third harmonic components.

When waveform given by equation (3.2), passes through (3.1), we have

$$e(t) = A_e sin(w_g t) + e_{h2}(t) + e_{h3}(t) \tag{3.4}$$

where A_e is the error amplitude of the fundamental component, and e_{h2} and e_{h3} are error components due to harmonic distortions as follows

$$\begin{aligned} e_{h2}(t) &= \lambda_{h2} sin(2w_g t) \\ e_{h3}(t) &= \lambda_{h3} sin(3w_g t) \\ \lambda_{h2} &= \frac{|w_0^2 - (2w_g)^2|}{\sqrt{(w_0^2 - (2w_g)^2)^2 + (2K_i w_g)^2}} A_{h2} \\ \lambda_{h3} &= \frac{|w_0^2 - (3w_g)^2|}{\sqrt{(w_0^2 - (3w_g)^2)^2 + (3K_i w_g)^2}} A_{h3} \end{aligned} \tag{3.5}$$

Squaring the error signal in (3.4), we have

$$\begin{aligned} e^2(t) &= (A_e sin(w_g t) + e_{h2}(t) + e_{h3}(t))^2 \\ &= f(w_0) + \frac{1}{2}\lambda_{h2}^2 + \frac{1}{2}\lambda_{h3}^2 + \Gamma(w_g, 2w_g, 3w_g, 4w_g, 6w_g) \end{aligned} \tag{3.6}$$

where Γ is sum of generated high frequency sinusoidals.

By passing (3.6) through the notch filter and removing double frequency components in Γ, we have

$$e^2(t)\Big|_{notch} = f(w_0) + \frac{1}{2}\lambda_{h2}^2 + \frac{1}{2}\lambda_{h3}^2 + \Gamma(w_g, 3w_g, 4w_g, 6w_g) \tag{3.7}$$

In (3.5), since the difference between resonant frequency and harmonic frequencies ($2w_g$ and $3w_g$) is large, the amplitude of the unwanted components in error signal in (3.4) are equal to the amplitude of the unwanted components in the input grid voltage. Thus, the following approximation can be made

$$\begin{aligned} \lambda_{h2} &\approx A_{h1} \\ \lambda_{h3} &\approx A_{h2} \end{aligned} \tag{3.8}$$

Considering (3.8), equation (3.7) can be rewritten as follows

$$e^2(t)\Big|_{notch} = f(w_0) + \frac{1}{2}A_{h2}^2 + \frac{1}{2}A_{h3}^2 + \Gamma(w_g, 3w_g, 4w_g, 6w_g) \tag{3.9}$$

The gradient of $f(w_0)$ is calculated by multiplying (3.9) with the perturbation signal as shown in Fig. 2.9 of the previous chapter. The resultant signal is thus expressed as

$$\begin{aligned} \dot{w_0}(t) = \frac{df(w_0)}{dw_0} &+ (\frac{1}{2}A_{h2}^2 + \frac{1}{2}A_{h3}^2)A_{esc}sin(w_{esc}t) \\ &+\Gamma(w_g, 3w_g, 4w_g, 6w_g)A_{esc}sin(w_{esc}t) \end{aligned} \tag{3.10}$$

As it can be seen in (3.10), only the first component is contributing to grid frequency estimation. Other components are generated by harmonic distortions. Since these components are not function of the resonant frequency, they do not contribute to frequency estimation. These components actually create oscillations on top of the estimated frequency as follows

$$\begin{aligned} w_0(t) + \int (\frac{1}{2}A_{h2}^2 + \frac{1}{2}A_{h3}^2)A_{esc}sin(w_{esc}t) \\ + \int \Gamma(w_g, 3w_g, 4w_g, 6w_g)A_{esc}sin(w_{esc}t) \end{aligned} \tag{3.11}$$

3.1.1 Notch Filters in Synchronization loop

To remove unwanted distortion from the estimated frequency in (3.11), notch filters are proposed that act at harmonic distortion frequencies in the synchronization loop as shown in Fig. 3.2a. To remove multiple harmonics from the grid, multiple notch filters can be cascaded. As it can be seen, the error signal feeding the FLL input is obtained from the output of the notch filters which has removed the unwanted grid harmonics. Therefore, the estimated frequency does not contain ripples and the estimated phase does not contain grid harmonics. The notch filters are also adapted to the frequency variations of the grid by feeding them the estimated frequency of the FLL. By employing this structure, the estimated phase of the grid at the output of the resonant filter does not contain harmonics. The bode plot of the closed-loop resonant filter with harmonic damping notch filters is

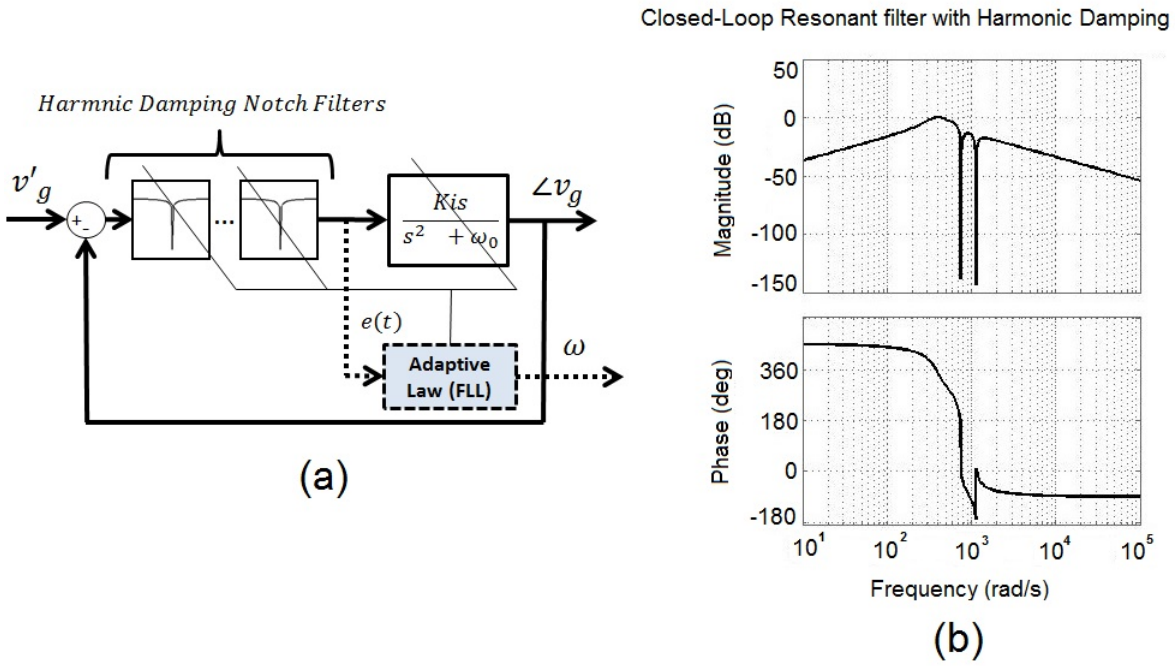

Figure 3.2: (a) Proposed synchronization block with harmonic damping notch filters (b) Bode diagram of closed-loop resonant filter with notch filters

shown in Fig. 3.2b. As it can be seen the notch filters at the harmonic frequencies are effectively damped.

3.2 Effect of Grid Distortion on Output Current

In the last section, a synchronization block was proposed which was able to remove the effect of unwanted harmonic from the estimated phase/frequency of the grid. In this section, the effect of the grid harmonic distortions on the PR current control loop will be investigated.

As it can be seen from the current control scheme proposed in previous chapter in Fig. 2.2, the reference current (i_{ref}) is derived from the FLL synchronization block. Synchronization block with harmonic damping notch filters inside its feedback loop, create a reference current signal (i_{ref}) which does not contain grid harmonic distortions.

However, that is not enough for the current controller to be able to perform flawlessly during the harmonic distortions. As already explained in chapter 2 of this thesis, the PR current controller is designed to only track the fundamental component of the reference current (i_{ref}) and fails to track the reference current at other frequencies. According to [51], PR current controllers cannot solely compensate grid harmonics due to their limited bandwidth. The controller's sensitivity to compensate other harmonics was modeled in [50]-[52]. To demonstrate this fact, the output current in the proposed PR current control

loop in Fig. 2.2 of the last chapter is described as follows

$$I_g(s) = G_{Load}G_{inv}G_{PR}(I_{ref} - I_g) - G_{Load}V_g \tag{3.12}$$

where G_{Load}, G_{inv} and G_{PR} are transfer functions of output filter, inverter and PR controller.

As it can be seen from (3.12), the output current is constructed from two signals: grid voltage and the reference current. Since I_{ref} is generated by the synchronization block which removes harmonic distortions, only the effect of grid voltage on the output current is studied here.

Th effect of the grid voltage on output current (I_g) can be studied by setting $I_{ref} = 0$ which yields to

$$\frac{V_g}{I_g} = -(\frac{1}{G_{Load}} + G_{inv}G_{PR}) \tag{3.13}$$

The equation (3.13) is called grid impedance. The large values of grid impedance makes the output current independent to grid voltage. Since PR controller is only able to track the reference signal at grid frequency, the output current is dependent to the harmonics presented at grid voltage and grid impedance is low at those frequencies.

To track the reference current (i_{ref}) at harmonic frequencies, the PR controller is modified as follows

$$G_{PR} = K_p + \frac{K_i s}{s^2 + w_0^2} + \frac{K_2 s}{s^2 + (2w_0)^2} + \frac{K_3 s}{s^2 + (3w_0)^2} \tag{3.14}$$

As it can be seen in (3.14), the modified PR controller has additional resonant filters tuned at harmonic frequencies. This filters track the reference current at other frequencies which make the output current independent to the grid voltage distortions. This additional resonant filters are often called Harmonic Compensation (HC) filters.

To demonstrate the effectiveness of HC filters, grid impedance of the modified PR controller in (3.14) and conventional PR controller in (3.13) are demonstrated at 2nd and 3rd harmonics frequencies in Fig. 3.3a. As shown, adding Harmonic Compensation (HC) resonant controllers at 2nd and 3rd harmonics, increase the value of grid impedance at those frequencies which make the current harmonics follow the reference current (i_{ref}) at those frequencies.

The harmonic compensation filters are added in parallel to the proposed PR control scheme as shown in Fig. 3.3b. As shown, the resonant frequency of the HC filters are also adapted with the estimated frequency of the proposed FLL to make the current control accurate during grid frequency fluctuations.

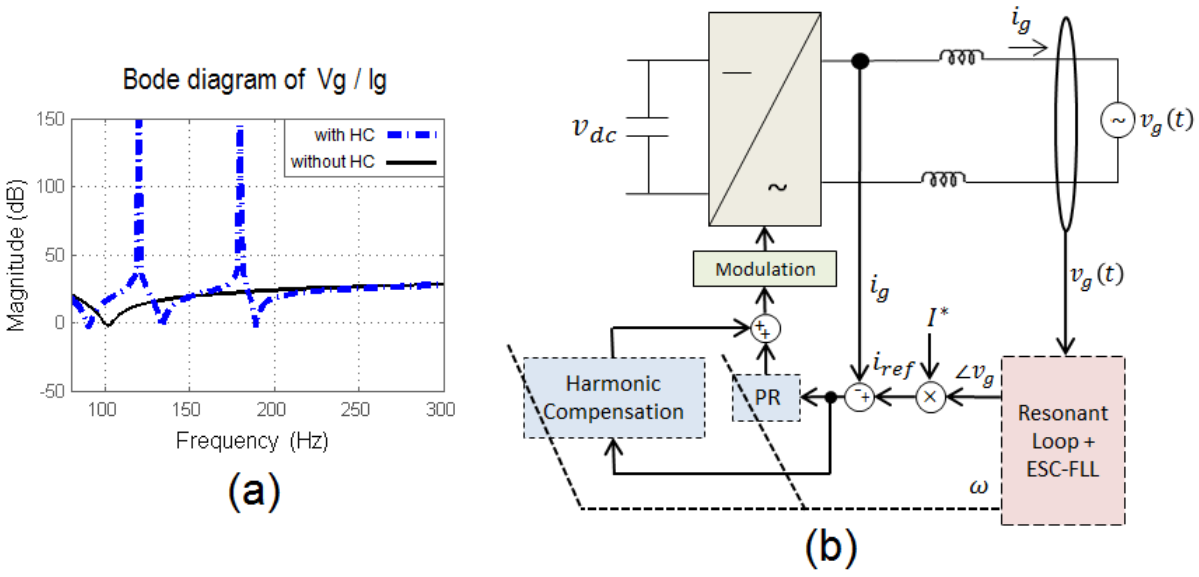

Figure 3.3: (a) Bode diagram of grid-impedance at harmonic frequencies (b) Current control system with addition of Harmonic Compensation (HC) filters

This chapter can be concluded as follows: by employing the modified version of the synchronization block to produce a accurate reference current (i_{ref}) from a distorted gird voltage and employing modified version of the PR controller to follow this reference signal at fundamental and harmonic frequencies, the generated output current (i_g) will have, a low value of THD, despite grid voltage distortions.

Chapter 4

Simulation Studies

For evaluating the performance of the proposed synchronization algorithm and the adaptive control system, simulation studies were conducted and the results are demonstrated. The control systems were designed and evaluated using Matlab/Simulink software. For modeling power electronic circuits, "SimPowerSystems" library was employed.

In this chapter, first the digital implementation of the control system will be discussed, then the simulation studies for validating the control systems of previous chapters will be be presented.

4.1 Digital Implementation

For digital implementation, first the transfer functions of the controllers described in the previous chapter should be converted from s-domain to state-space representation. In time-domain, a general dynamic system is expressed as follows

$$\begin{aligned} \dot{x}(t) &= f(t, u, x) \\ y &= g(t, u, x) \end{aligned} \tag{4.1}$$

where x is the state of the system, u is the input of the system and y is the output of the system.

In (4.1), the dynamic system is described by a sets of states expressed by first order differential equations. This dynamic system is then discretized digitally by approximating the continuous-time differential equations in discrete time as follows

$$\begin{aligned} x_{n+1} &= f'(t_n, u_n, x_n) \\ y_n &= g'(t_n, u_n, x_n) \end{aligned} \tag{4.2}$$

where n is an integer representing the discretized time, f' and g' are the approximation to calculate the next value of the state. This two functions are calculated based on the discretization method used.

The most important aspect of discretizing the control system is to make sure the method can accurately approximate continuous-time dynamics. Otherwise, the states in the discretized system will not converge to the values of continuous time states and the system might become unstable.

4.1.1 Discretization of Synchronization Block

The synchronization block proposed in the second chapter of this thesis, is a closed-loop resonant filter with a novel extremum-seeking FLL. The open-loop resonant filter can be expressed in terms of two first order differential equations as follows

$$\begin{aligned} \dot{x}_1 &= x_2 \\ \dot{x}_2 &= u(t) - w_0^2 x_1 \end{aligned} \tag{4.3}$$

where w_0 is the resonant frequency of the resonant filter.

These differential equations can be discretized using the Tustin or Backward Euler (with step delay) methods [36], [37], [38]. However, according to [38], since the Tustin transformation is nonlinear, the frequency axis is compressed and the poles are displaced. Thus, Tustin with frequency pre-wrapping is suggested. The pole locus of discretized resonant controllers are analyzed in [37].

The proposed synchronization block in Fig. 2.6 with the extremum-seeking loop is nonlinear and non-stationary dynamic system. The state-space representation of the synchronization block is expressed as

$$\begin{aligned} \dot{x}_1 &= x_2 \\ \dot{x}_2 &= K_i(u - x_2) - x_1\big[2\pi\big(x_3 + a_{es} sin(x_6)\big)\big]^2 \\ \dot{x}_3 &= 2K_{es}\big[(u - x_2)^2 - x_5\big] sin(x_6) \\ \dot{x}_4 &= x_5 \\ \dot{x}_5 &= 2\xi w_n (u - x_2)^2 - w_n^2 x_4 - 2\xi w_n x_5 \\ \dot{x}_6 &= 1000\pi \end{aligned} \tag{4.4}$$

where K_{es} is the extremum seeking gain, a_{es} is the amplitude of the perturbation signal, K_i is the gain of the resonant filter, ξ is the damping factor of the notch filter in the extremum-seeking loop and w_n is the resonant frequency of this notch filter which is a fixed value and is equal to the nominal frequency of the gird.

In (4.4), x_3 is the estimated frequency of the grid which is fed to the resonant filter described by x_1 and x_2. x_4 and x_5 are representing the notch filter used to extract the squared amplitude of the error signal. x_6 is the phase of the perturbation signal. As it can be seen the perturbation frequency is chosen to be $(2\pi \times 500)rad/s$.

To discretize the synchronization block represented by nonlinear dynamic system in (4.4), Runge-Kutta fourth order discretization algorithm (RK4) is employed.

The solver approximates the next states of the dynamic system by calculating the $f(t, x, u)$ represented in (4.3), twice in a middle point of the time-step (V_2 and V_3), once in the current time-step (V_1) and once in the next step-time (V_4). It should be noted that the current time-step is nT where T is a time-step. The next time-step is $(n+1)T$ and the mid-point of the time-step is $nT + \frac{nT}{2}$.

Then the next state is calculated by adding the weighted average of the calculated components to the current state as follows

$$x_{n+1} = x_n + \frac{h}{6}(V_1 + 2V_2 + 2V_3 + V_4) \tag{4.5}$$

$$\begin{aligned} V_1 &= f(t_n, x_n) \\ V_2 &= f(t_n + \frac{h}{2}, x_n + \frac{h}{2}V_1) \\ V_3 &= f(t_n + \frac{h}{2}, x_n + \frac{h}{2}V_2) \\ V_4 &= f(t_n + h, x_n + hV_3) \end{aligned} \tag{4.6}$$

The mechanism of the solver is demonstrated in Fig. 4.1a. As it can be seen, four components of the method are calculated in two computational sampling time. After all four components are calculated, the next state is approximated by the equation (4.6). Therefore, each discretization time-step takes two computational sampling time.

The RK4 discretized FLL was implemented using Embedded function in Matlab/Simulink. The pseduo-code of the algorithm is demonstrated at Fig. 4.1b.

Adding the harmonic damping notch filters inside the synchronization block will only increase the number of dynamic states depending on the number of notch filters cascaded in the loop. This modified version of the synchronization block which was represented in Fig. 3.2a in the previous chapter is also discretized using RK4 method.

4.1.2 Discretization of Controller Blocks

The dynamic system of the PR controller can also be represented by the state-space equations similar to (4.3). PI controller dynamics can be represented by one state. To ensure the performance of the digital controller, both PI and PR controllers were discretized by

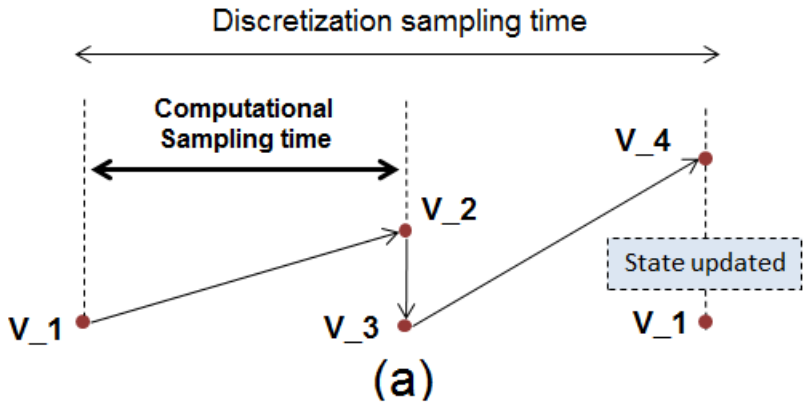

(a)

1. All the variables initialized

2. At the initial computational loop, the first RK4 item for the next state update is calculated as follows

```
v1_x1 = x2     // at initial state only the first
                  component is calculated
...
```

3. At the second computational loop in mid-point state, two midpoint RK4 components are calculated as follows

```
v2_x1= x2+(T/2)*v1_x2;   // second and third
                            components of the RK4
                            is calculated
...
v3_x1= x2+(T/2)*v2_x2;
...
```

4. At the third computational loop in state-computation state, last component calculated and state updated

```
v4_x1 = x2+T*v3_x2;    // last component of RK4 is
                          calculated
...
x1 = x1 +  (T/6)*(v1_x1+2*v2_x1+2*v3_x1+v4_x1);
                                   // states updated
...
v1_x1 = x2;      // the first component of the next
                    state is calculated
```

5. The procedure in an infinite loop is handed to the (3) and then (4) again.

(b)

Figure 4.1: The Rungge-Kutta 4th discretization method: (a) Block diagram (b) Sequential pseudo-code

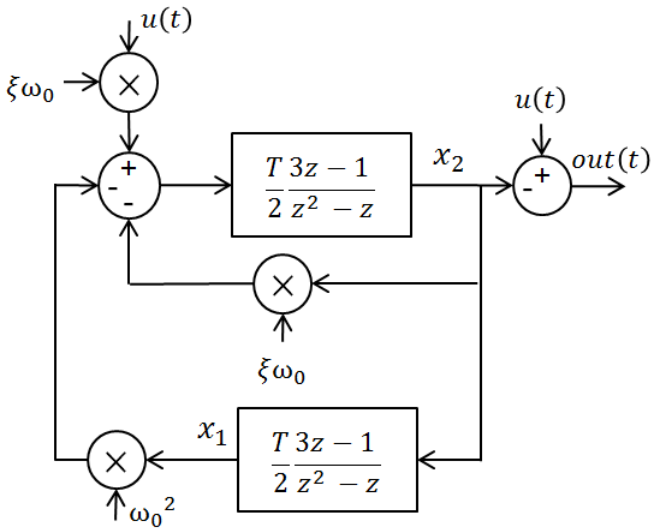

Figure 4.2: Block diagram of the discretized notch filter using Adams-Bashforth method

Parameters	Simulation Value
Resonant gain (K_i)	200
Extremum-Seeking Gain (K_{es})	-125000
Perturbation amplitude (a_{es})	2
Perturbation frequency	500Hz
Damping factor of notch filter ξ_{es}	2
Resonant frequency of the notch filter	120Hz

Table 4.1: Synchronization block parameters

RK4 method as well. However, for implementing the notch filter to remove the DC-link ripples, Adam-Bashforth method was employed due to its superior accuracy [60].

The block diagram of the discretized notch filter for removing DC-link ripples using Adam-Bashforh method is shown at Fig. 4.2 where $u(t)$ is the input to the filter, $out(t)$ is the output, T is the discretization time-step, w_0 is the resonant frequency of the notch filter which is adapted to be twice the estimated frequency of the FLL and ξ is the damping factor of this notch filter.

4.2 Adaptive PR Current Controller Simulations

Simulations were conducted to validate the proposed adaptive PR control algorithm shown in Fig. 2.2 of chapter two of this thesis. Using a discrete simulation helps to evaluate the behavior of proposed system when implemented on a micro-controller device.

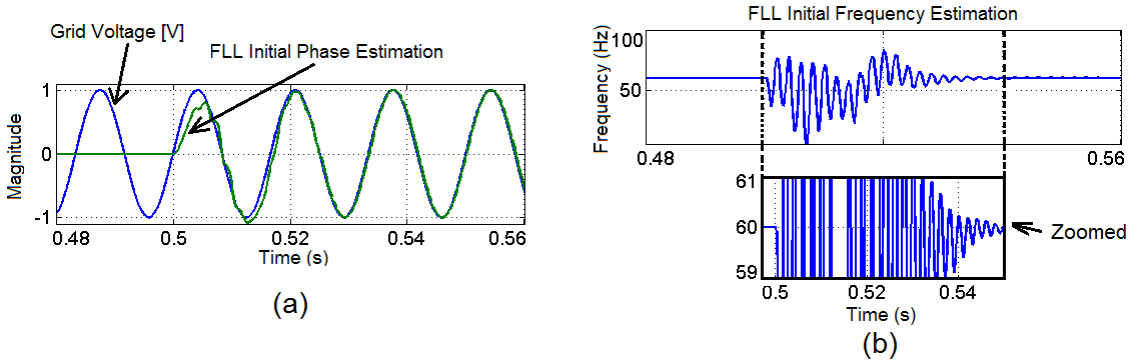

Figure 4.3: (a) Phase estimation transient at the start-up of FLL (b)Frequency estimation transient of FLL in the start-up

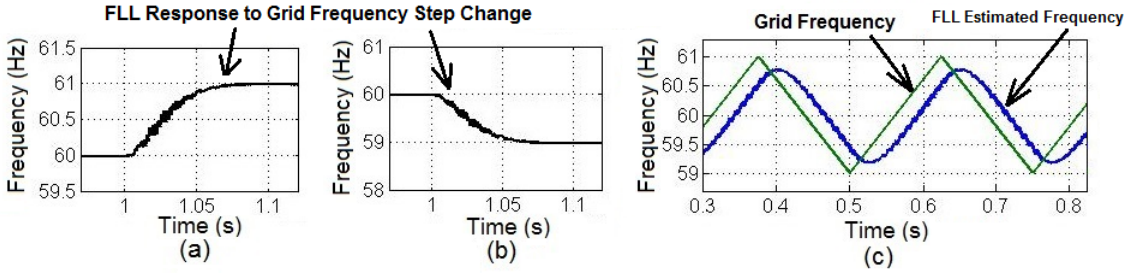

Figure 4.4: FLL frequency tracking response to (a) Grid frequency step change to 61Hz (b) Grid frequency step change to 59Hz (c) Grid frequency ramp changes

4.2.1 Frequency Tracking of Proposed FLL

Before evaluating the performance of the adaptive PR controller, the performance of the proposed synchronization block is evaluated. The parameters used for the synchronization block were achieved by extensive simulations and are shown in Table 4.1.

Choosing parameters is a trade-off between the stability of the system and the transient response in estimating the phase/frequency of the grid. The resonant feedback loop of the FLL should be faster than the extremum-seeking loop as discussed in Chapter 2. On the other hand, high values of this gain, makes the frequency estimation loop sensitive to phase jumps in the grid voltage. As it can be seen from Table 4.1, the damping factor of the notch filter was chosen large in order to make the bandwidth of the notch filter wide enough to be insensitive to grid frequency changes. The resonant frequency of this notch filter was fixed to twice the nominal grid frequency.

First, the initial transient response of the FLL is demonstrated as shown in Fig. 4.3. As it can be seen, at the time $t = 0.5$ second, the FLL was activated. It approximately took three cycles for the FLL to estimate the phase and frequency of the grid. It should be noted that phase and frequency estimation times are almost equal. It is due to the fact that the

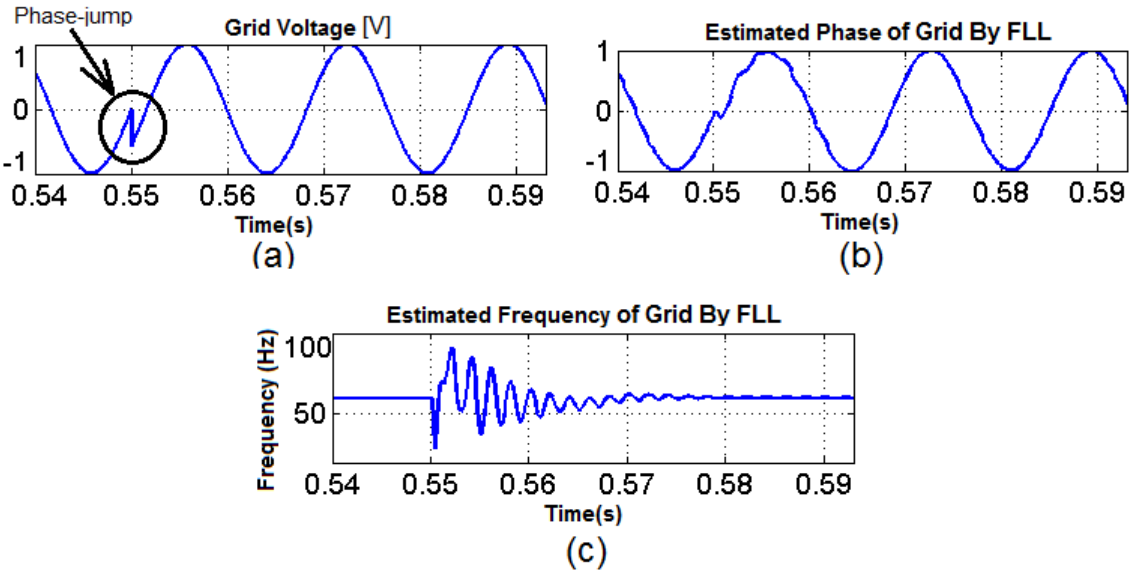

Figure 4.5: FLL response to -270deg phase jump (a) Grid voltage (b) Estimated phase by FLL (c) Estimated frequency by FLL

phase error between the input/output of the closed-loop resonant filter is dependent on the frequency difference between grid frequency and the resonant frequency.

The frequency estimation performance of the proposed FLL is demonstrated in Fig. 4.4. The response of the proposed FLL to 1Hz step change in grid frequency is shown in Fig. 4.4(a) and Fig. 4.4(b). The transient response of the FLL for frequency estimation is approximately 80ms. The response of the FLL to a continuous frequency disturbance is shown in Fig. 4.4(c). As shown, the FLL is tracking the frequency of the grid with transient time of almost 10ms. As previously mentioned, fast frequency estimation of the grid is required not only for adapting the PR controller but also for monitoring the grid frequency. According to IEEE 1547 standard, the grid-tied power generation systems should react to abnormalities in grid frequency within a pre determined time-frame.

The transient response of the proposed FLL to a -270 degree phase-jump in the grid voltage is demonstrated in Fig. 4.5. At the time $t = 0.55$ second the phase jump was applied. It took almost two cycle for the FLL to synchronize the inverter with grid voltage.

4.2.2 Current Controller Simulation

The performance of the adaptive PR controller is demonstrated in this section. The proportional and resonant gain of the PR controller should be chosen to provide fast transient response. However, a very wide bandwidth current controller makes it more vulnerable to distortions. Also if harmonic compensation resonant filters are used in the PR controller, high gains of resonant filters might make the system unstable since their bandwidths might

Parameters	Simulation Value
Resonant gain of PR (K_i)	100
Proportional gain of PR (K_p)	0.5
Filter inductance (L)	15mH
Grid voltage (V_g)	20V(peak-peak)
DC input voltage (V_{dc})	20V DC
Frequency of unipolar SPWM modulation	10 KHz

Table 4.2: The Current control system parameters

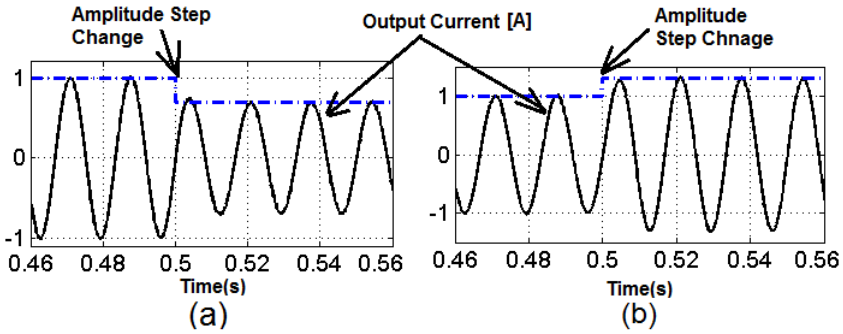

Figure 4.6: PR current controller simulation results (a) Initialization (b) Response to positive step change in reference current (c) Response to negative step change in reference current

interference with each other. The parameters of the power electronic circuits and the PR current controller are demonstrated in Table 4.2.

As it can be seen, the grid voltage was stepped down to 20V (peak-to-peak) due to the experimental limitations. To compare simulations with experimental results, same parameters for control system and power electronic circuits are used. In the current control system, since the control-loop on DC-link was not used, it is assumed that the input to the inverter is a DC source voltage. The value of this source was chosen to be 20V which is enough to provide and inject an AC current with the amplitude of 1 Amp into the grid.

The initial transient time for the PR controller to synchronize itself with the grid voltage was 70ms. The response of the PR controller to a step change in the reference signal amplitude is demonstrated at Fig. 4.6(a) and (b). It took 50ms for the system to respond to the step change.

Another issue was the proper performance of the current controller during grid frequency variations. The simulation results of the non-adaptive PR controller working at 61Hz is shown in Fig. 4.7(a). As it can be seen, the grid frequency variation creates a phase-shift in the injected current to the grid. The adaptive PR controller working at 61Hz, is shown in Fig. 4.7(b) with almost no phase-shift in the output current. The small phase-shift in output

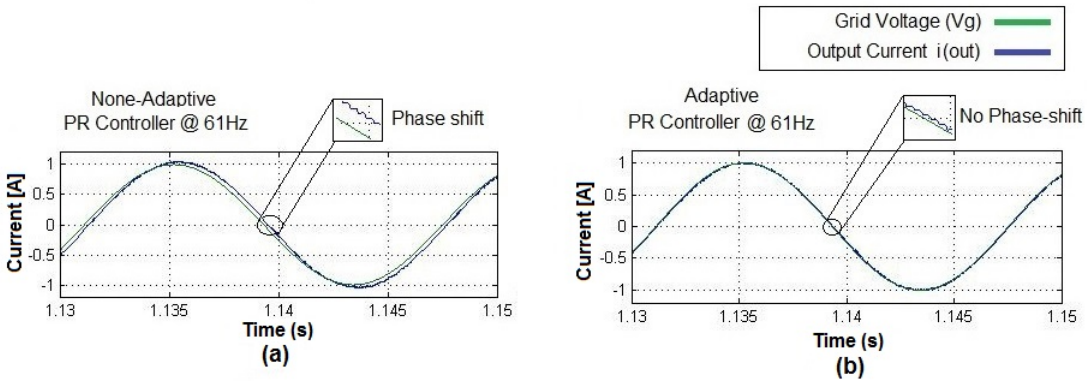

Figure 4.7: Response of current controller working at 61 Hz (a) Non-adaptive PR (b) Adaptive PR

current of the adaptive PR controller is due to additional current harmonics (especially third harmonic due to DC-link double frequency ripple) and discretization inaccuracies.

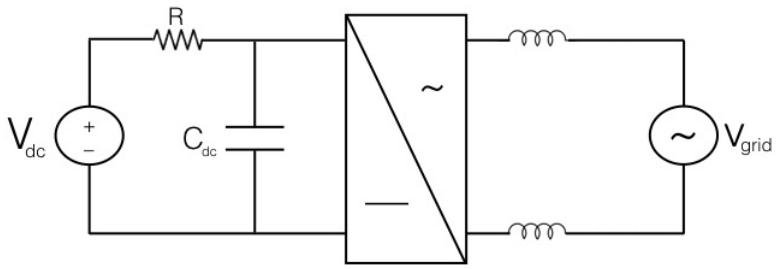

Figure 4.8: The power electronic circuit to emulate the DC/DC converter at the DC-link

Parameters	Simulation Value
Integral gain of PI (K_i)	-10
Proportional gain of PI (K_p)	-0.5
DC-Link capacitance (C_{dc})	200uF
Emulation resistance (R)	9Ohm
Emulation DC source (V_{dc})	20V DC
Notch filter damping factor	0.7

Table 4.3: The voltage regulation control parameters

4.3 PI Voltage Controller Simulation

In this section, the performance of the voltage control loop is evaluated. To emulate the current coming from the DC/DC converter to the DC-link capacitor, a DC voltage source in series with a resistor is used as shown in Fig. 4.8. The parameters of the power electronic circuit and the PI voltage controller are demonstrated in Table 4.3.

The high PI controller gain will provide faster transient response but also will increase the bandwidth of closed-loop voltage controller. In conventional PI control loops, large bandwidth will let all the DC-link double frequency ripples pass into the control loop which will increase the THD of the output current. However, in the proposed voltage control loop, this issue was solved by using an adaptive notch filter to remove the double frequency ripples as it is already shown in Fig. 2.12 in Chapter 2 of this thesis.

The initial transient response of the PI voltage control loop is shown in Fig. 4.9. As it can be seen, the DC-link voltage contains considerable amount of double frequency ripple. The adaptive notch filter removes this ripple distortion effectively as shown in Fig. 4.9(b). The transient response of initialization is 200ms with the chosen value of the PI parameters.

The response of the PI voltage control loop to a step change in the reference voltage is demonstrated in Fig. 4.10. At $t = 1$ second, the reference DC-link voltage value is changed from 17Volt to 18Volt. As it can be seen from the Fig. 4.10(b), the DC-Link voltage reaches this value with the transient time of 100ms. It should be noted, to regulate the DC-link voltage at a higher value, the amplitude of the output current is reduced.

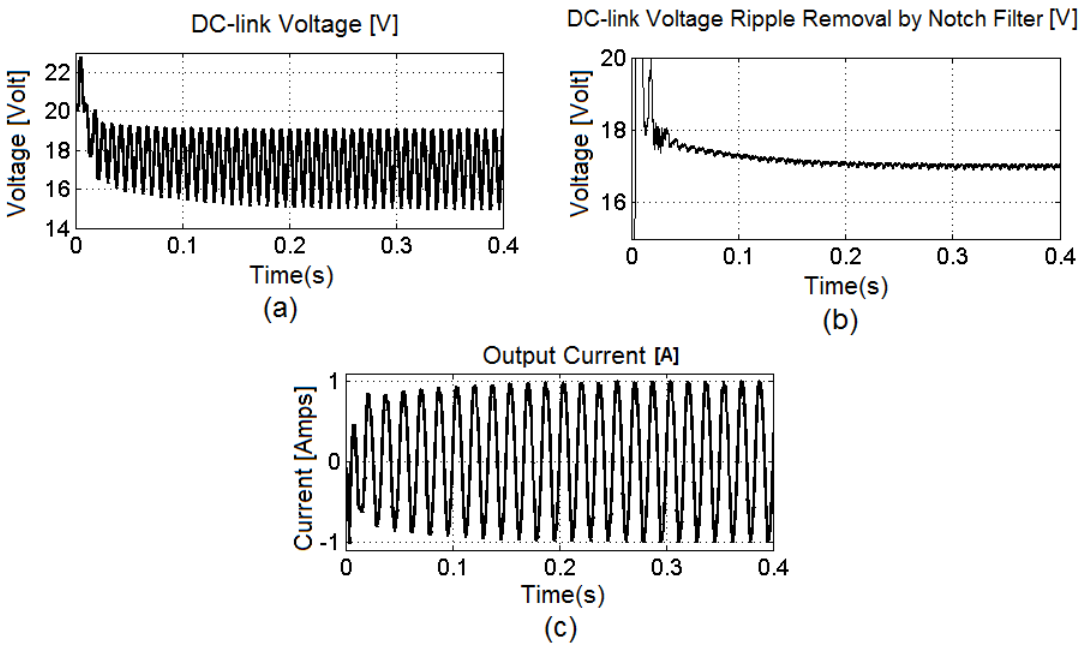

Figure 4.9: DC-link initial transient response: (a) DC-link voltage (b) Output of adaptive notch filter to remove double frequency ripple (c) Output current

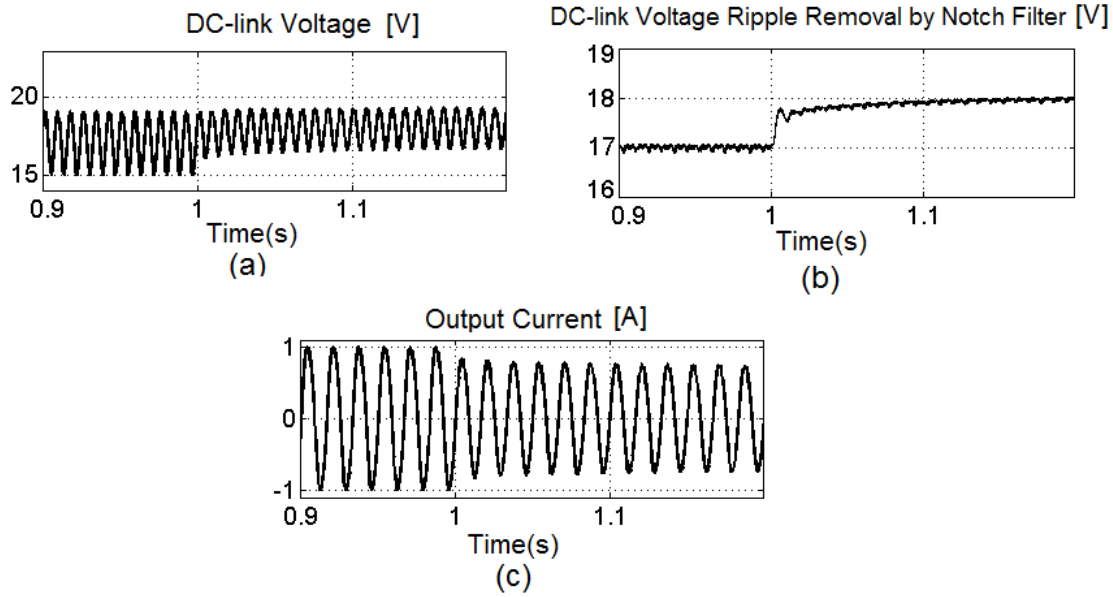

Figure 4.10: DC-link transient response to step change: (a) DC-link voltage (b) Output of adaptive notch filter to remove double frequency ripple (c) Output current

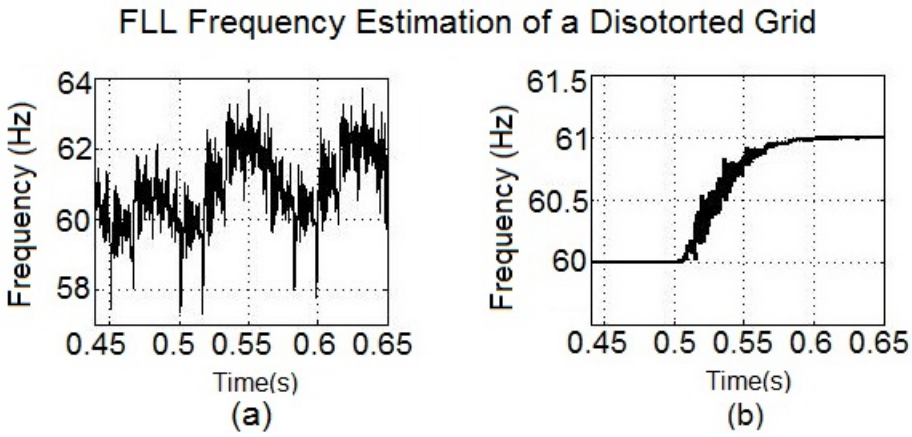

Figure 4.11: Frequency estimation of FLL in a distorted grid: (a) Without harmonic damping notch filters (b) With harmonic damping notch filters

4.4 Grid Harmonic Distortions Simulation

To demonstrate the effect of grid harmonic distortions on the control system and evaluate the proposed control scheme in chapter 3 of this thesis, simulation studies are conducted.

In this section, it is assumed that the grid is distorted with 7% 2nd harmonic, 6% 3rd and 5% 4th harmonic with a THD of 10.49%. These harmonics represent low frequency harmonic distortions which affect the control system more than higher order harmonics. High harmonic distortions are usually attenuated partially by the second order filters in the control scheme and synchronization block.

The effect of harmonic distortions on the FLL synchronization block is demonstrated in the simulation results in Fig. 4.11 . At the simulation time 0.5s in Fig. 4.11, a 1Hz step change is introduced to demonstrate frequency adaptability of the proposed FLL. As it can be seen from Fig. 4.11 (a), adding distortion to the FLL without notch filters, creates ripples on top the estimated frequency. This result validates the analysis provided in chapter 3. Adding cascaded notch filters effectively eliminates the ripples and increases the accuracy as shown in Fig. 4.11(b). With harmonic damping notch filters in the FLL loop, the estimated phase of the grid had the THD of 0.29%.

Also, harmonic distortions affect the quality of the output current. By adding a harmonic compensation resonant filter to the PR controller at the 2nd, 3rd, 4th and 5th harmonic frequencies and using cascaded notch filters in the FLL loop, the THD of output current is reduced to 0.79%. It should be noted that if harmonic compensations are removed from the PR current controller, but the notch filters are used in the FLL loop, the output current THD is increased to 6.47%. This is despite the fact that the estimated phase of the grid by synchronization block does not contain any harmonics.

Chapter 5

Experimental Results

In this chapter, the control systems proposed in chapter 2 and chapter 3 of this thesis are experimentally evaluated and the results are presented.

5.1 Experimental Setup

The proposed experimental setup is shown in Fig. 5.1. The Texas Instrument DRV8305 three-phase gate driver was used as the inverter for the proposed system.

To emulate frequency variations in a grid-connected system, a programmable AC source (GW INSTEK) was connected to a power amplifier. The AC source and the power amplifier created a 4-quadrant AC generator which is able to deliver/receive considerable amount of current. The power amplifier was created using an linear operational amplifier (Power Amp Design's PAD127 OPAMP) in a negative feedback loop as shown in Fig. 5.1(c). Since push/pull amplifier was used in the last stage of the employed OPAMP, the power amplifier is able to receive the generated current from the inverter.

To emulate grid harmonic distortions, two other AC sources were added to the fundamental programmable AC source used to emulate the grid by an AC voltage adder circuit. To determine the quality of the produced current, Tektronix PA1000 power analyzer was used to monitor power factor and harmonic spectrum.

The digital implementation of the continuous controllers was explained in the last chapter. These discrete algorithms were implemented with the Texas Instrument F28335 Experimenter Kit which has maximum clock speed of 150MHz. To program the controller in this MCU, MATLAB Embedded Coder and Real-time Workshop software was used. By using this tool, the same control blocks designed in simulation studies were used to program the MCU. The sampling frequency of 14KHz was used for the digital controllers. Trade-off for choosing the sampling frequency was between the accuracy of the digital controller and the microprocessor overrun. CPU overrun occurs when the length of the program cannot be executed with specified speed of execution (sampling frequency).

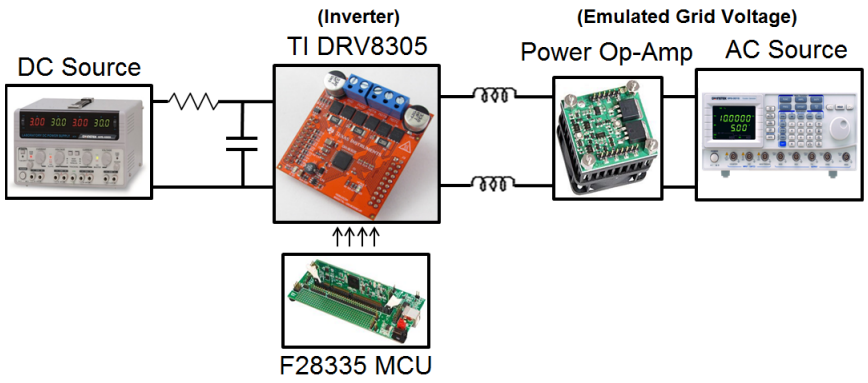

(a)

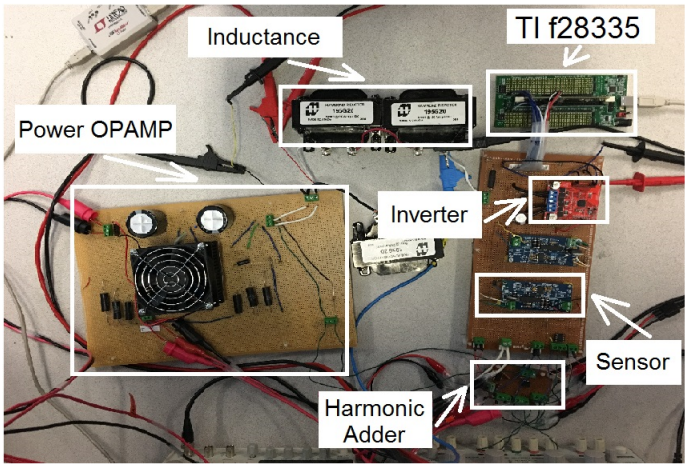

(b)

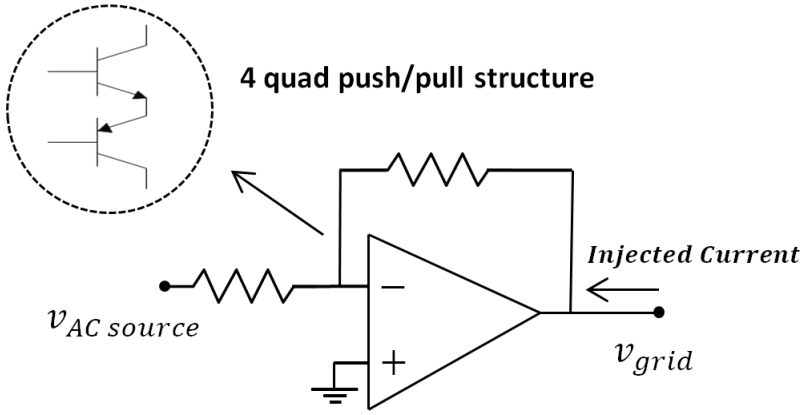

(c)

Figure 5.1: The proposed experimental setup (a) Block diagram (b) Implemented power electronics (c) Power amplifier used to emulate grid voltage

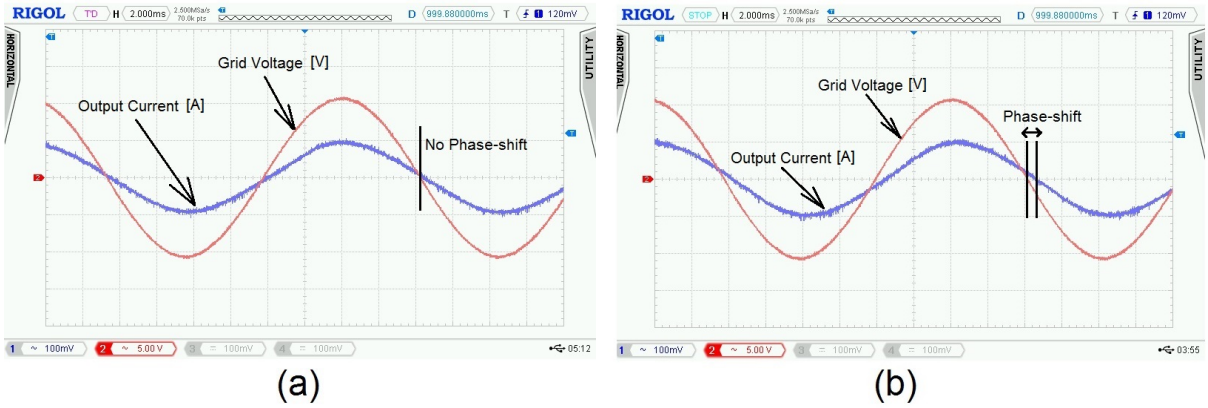

(a) (b)

Figure 5.2: (a) Response of adaptive PR controller working at 61Hz (b) Response of non-adaptive PR controller working at 61Hz (2ms per unit)

The estimated parameters by the control loop were read using serial communication (SCI) with the micro-controller. The data was read in the computer using Matlab/Simulink embedded coder host.

Also it should be noted that the same design parameters for the controllers and power electronic circuits are used as it was mentioned in the simulation results in previous chapter.

5.2 Adaptive Current Controller

To determine the validity of the adaptive PR current controller, the frequency of the AC signal source was changed to 61Hz in order to compare the performances of adaptive PR and non-adaptive PR controllers. The responses of the system were captured as shown in Fig. 5.2. As it can be seen from Fig. 5.2(a), the output current of the adaptive PR controller operates at the 61Hz grid frequency without a phase-shift. This means that the resonant frequency of the PR controller is adapted to the calculated frequency by using the proposed FLL. For comparison, the response of non-adaptive PR controller working at 61Hz grid frequency is also shown in Fig. 5.2(b). As it can be seen, a phase-shift was created because the resonant frequency of PR controller is different than grid frequency. The amount of phase-shift is related to the bandwidth of the current controller. If the system has a higher bandwidth, the output current is less sensitive to the frequency variations. However, a very wide band PR controller loses its harmonic selectivity and is more vulnerable to grid harmonic distortions.

At a nominal frequency of 60Hz for both adaptive/non-adaptive current controllers, the Power Factor (PF) is measured at 0.993. At the 61Hz, the adaptive current controller had a PF of 0.993, while the output current of the non-adaptive PR controller had a PF of 0.981. PF dropped more slowly below 60Hz in comparison with frequencies above 60Hz. At 57Hz,

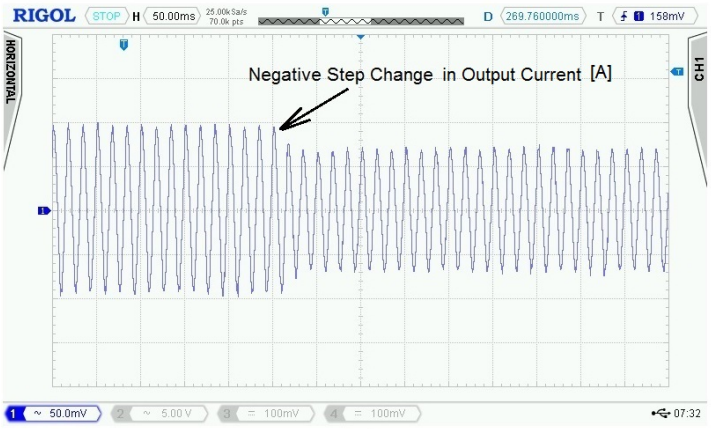

(a)

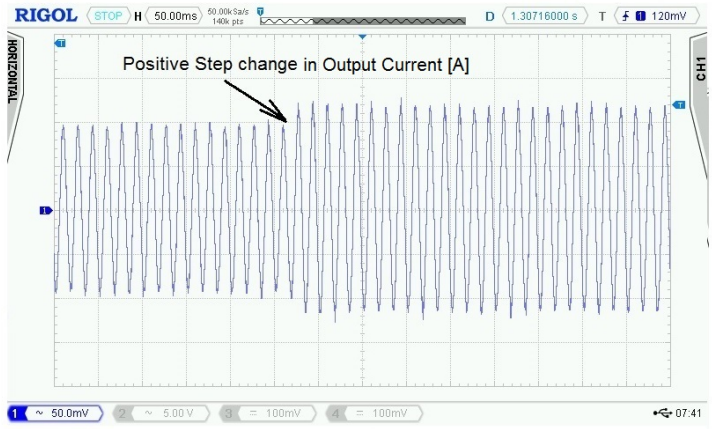

(b)

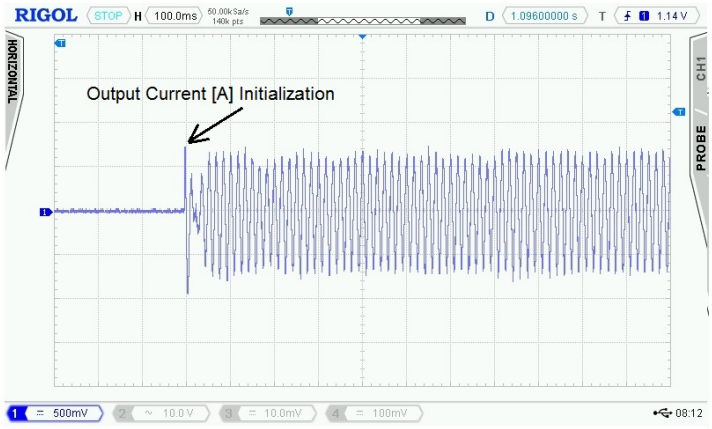

(c)

Figure 5.3: Response of adaptive PR controller to negative step change (50 ms per unit) (b) Response of adaptive PR controller to negative step change (50 ms per unit) (c) PR controller start-up response (100 ms per unit)

the non-adaptive PR controller has a PF of 0.983 and the amplitude of current was dropped by 20% percent.

The transient response of PR controller is demonstrated in Fig. 5.3. As it can be seen, it takes less than 100ms for current controller for synchronization with the grid. The response of the controller to negative and positive step change in reference current is shown in Fig. 5.3(a) and Fig. 5.3(b). The transient time was less than 50ms.

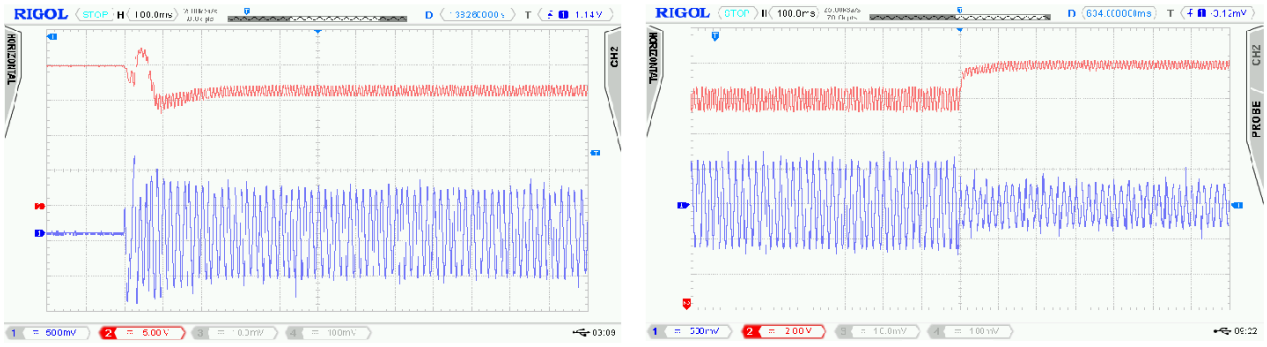

Figure 5.4: (a) Start-up response of voltage control loop (100 ms per unit) (b) Response of voltage controller to a step change in reference voltage (100 ms per unit)

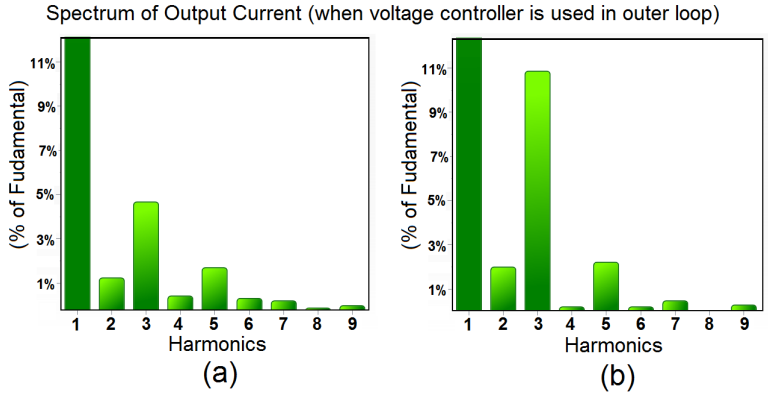

Figure 5.5: Spectrum of output current with outer voltage control when (a) Adaptive notch filter was used in voltage control loop (b) Adaptive notch filter was not used in voltage control loop

5.3 PI Voltage Controller

The performance of the PI voltage controller, proposed in Fig. 2.10 in chapter 2 of this thesis is presented in this section.

The transient performance of the PI controller is shown at Fig 5.4. At the start-up, the PI controller took $200ms$ to settle. As shown, adding PI control loop will affect the initial transient response of the current controller and increases its transient time to approximately $200ms$. The response of the system to a step-change in the reference voltage from 16.5Volt to 18.5Volt is shown in Fig. 5.4(b). As it can be seen, transient time was less than $100ms$.

The effect of double frequency ripple on the output current is shown in Fig. 5.5. As shown, the notch filter effectively attenuates the 3rd and 5th harmonics and reduce the THD of output current. Without notch filter, double ripple frequency at DC-link will increase the odd harmonics in output current with THD above 10%. The THD of the output current

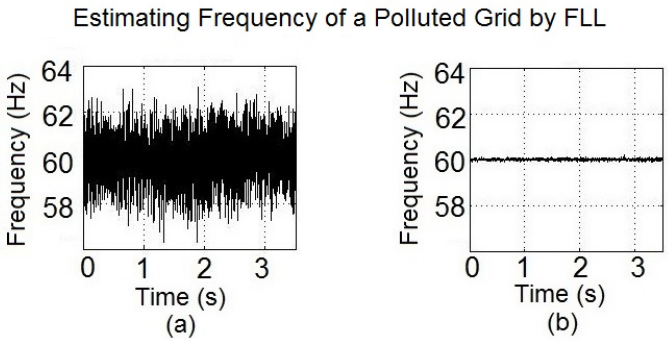

Figure 5.6: FLL frequency estimation of a distorted grid monitored by real-time SCI communication (a) Proposed control scheme without harmonic damping and regulation (b) Proposed system with harmonic damping and regulation

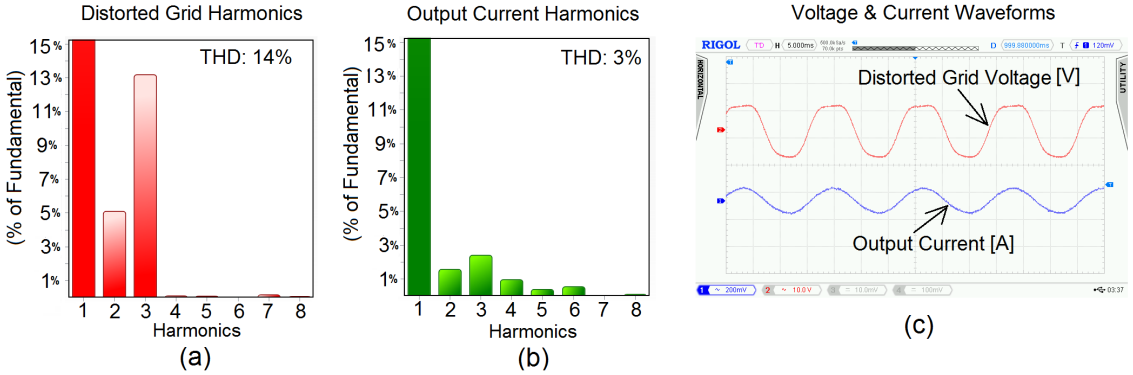

Figure 5.7: (a) and (b): Harmonic spectrum of grid voltage and output current (c) Voltage and current waveforms (5 ms per unit)

can be further attenuated by using harmonic compensation filters in the structure of the PR controller.

5.4 The Effect of Grid Harmonic Distortions

In this section, the proposed controller in chapter 3 is experimentally evaluated to determine its ability to reject grid harmonic distortions and produce high quality output current.

To experimentally validate the controller, 5% 2nd harmonic and 13% 3rd harmonic (overall grid voltage THD of 14%) were added to the grid voltage to emulate distortion. The calculated frequency was monitored at the output of the synchronization block by SCI communication with a host-computer. As expected, FLL without cascaded notch filters added ripples to the calculated frequency as shown in Fig. 5.6(a). Adding two notch filters at the second and third harmonics in the synchronization loop effectively attenuated the ripples as shown in Fig 5.6(b).

To ensure, the quality of the injected power to the grid, harmonic compensation (HC) blocks were added to the PR controller. Thus, the grid voltage harmonics do not affect the grid current harmonics. For this particular controller 2nd, 3rd, and 5th harmonic frequencies were compensated.

The response of the control system is shown in Fig. 5.7. The harmonic spectrum of grid voltage and output current is demonstrated in Fig. 5.7(a) and (b) measured via the power analyzer. The voltage and current waveform is shown in Fig. 5.7(c). As it can be seen, although the grid voltage was distorted, the THD of the output current was 3%. Without using harmonic compensations in the current controller and notch filters in the FLL synchronization block, the THD of the output current was increased to 8.7% which is above the requirement of IEEE 1547 for output current THD.

Chapter 6

Conclusion

6.1 Summary

This thesis presented adaptive control/synchronization of single-phase grid-connected inverters. It was shown that the interest in distributed micro-grid power generation systems has increased recently by improvements in cost/capacity of renewable energy power generation systems. The main integration challenge of these distributed systems is maintaining/regulating the stability of the grid by performing advanced monitoring and control strategies. The control system should react according to the regulatory standards in face of grid frequency/voltage abnormalities to ensure the grid stability and quality of the injected power to the grid.

In this thesis, performance of the inverter control scheme during frequency variations of the grid and harmonic distortions of the grid are analyzed.

First, the failure of the PR controllers to accurately regulate amplitude and phase of the injected current into the grid during frequency variations was demonstrated. A synchronization method (ES-FLL) was proposed based on a closed-loop resonant filter derived from internal model principle. This method, provides fast estimation of the grid's frequency/phase. An adaptive PR controller is proposed which uses the estimated frequency of the grid (by FLL) to perform properly during grid frequency variations.

Second, the effect of grid distortions on the quality of injected current was studied. The proposed control scheme can perform in a polluted grid by reducing distortions in output current. Its performance under distorted grid was analyzed and adaptive filters are added to its structure to remove the unwanted components from the estimated frequency/phase of the grid. By adding harmonic compensations to PR current controller, the output current was immunized to the harmonics presented in the grid voltage. Since the system is adaptive with the estimated frequency of the FLL, it works properly during frequency variation of the grid.

Also, a PI controller was used to regulate the DC-link voltage and control the flow of active power to the grid. It was shown that the double frequency ripples on DC-link voltage can reduce the quality of the output current. An adaptive notch filter was proposed in the voltage control loop to remove this double frequency component and enhance the quality of the output current. The resonant frequency of this notch filter was adapted to grid frequency variations by the proposed FLL synchronization block.

Simulations were performed by Matlab/Simulink and experimental setup was developed in lab to validate the performance of the proposed control system. It was shown that the adaptive PR controller creates an output current with almost no phase-shift with grid voltage during frequency variations of the grid. The ability of the synchronization block to estimate the grid frequency/phase components was demonstrated. As expected, grid harmonic distortions created ripples on top of the estimated frequency of the grid which was effectively removed by using adaptive filters in the synchronization block. Also, by using harmonic compensation filters in the PR controller, the THD of the output current was reduced to 3% during grid harmonic distortions.

The controller, consisting of FLL and adaptive PR controller, were discretized using the Runge-Kutta 4-th order method which resulted in good convergence characteristics when implemented on a digital microcontroller with a 14 kHz sampling time.

6.2 Future Work

This work can be further developed in the future. The suggestion are as follows

1. *Reactive Power Control*: In this thesis for achieving maximum power factor (PF), the output current was in-phase with grid voltage. However as mentioned before, injecting reactive power to the grid might be beneficial during grid instability. This work can be further developed to control the amount of active/reactive power injected to the grid.

2. *Islanding Mode Control*: In a micro-grid, if the power-generation is disconnected from the utility grid, it still can provide power to the local loads which is called working in Islanding Mode. This work can be further improved to be able to switch to islanding mode if the system is disconnected from the grid.

3. *LCL Filter with Resonant Damping*: The output filter of the inverter in this work can be improved to an LCL Filter with damping of its resonant frequency.

Bibliography

[1] U.S. Department of Energy, Revolution Now report (2016 update): The Future Arrives for Five Clean Energy Technologies. [Online]. Available: https://energy.gov/eere/downloads/revolutionnow-2016-update

[2] Jess Shankleman and Chris Martin, "Solar Could Beat Coal to Become the Cheapest Power on Earth", Bloomberg, Jan 2017. [Online]. Available: https://www.bloomberg.com/news/articles/2017-01-03/for-cheapest-power-on-earth-look-skyward-as-coal-falls-to-solar

[3] "Wind and solar advance in the power war against coal", Economist 2016. [Online]. Available: http://www.economist.com/news/finance-and-economics/21709355-clean-energy-surges-so-does-price-coal-wind-and-solar-advance-power

[4] Peter Rive, "Island in the Sun", SolarCity Blog 2016. [Online]. Available: http://blog.solarcity.com/island-in-the-sun/

[5] Eltawil, Mohamed A., and Zhengming Zhao, "MPPT Techniques For Photovoltaic Applications," *Renewable and Sustainable Energy Reviews 25 (2013)* 793-813.

[6] Brian B. Johnson, "Control, Analysis, and Design of Distributed Inverter Systems", PhD Dissertation, University of Illinois, Urbana 2013.

[7] "Products and solutions for solar energy", STMicroelectronics, Aug 2012. [Online]. Available: http://www.st.com/content/ccc/resource/sales_and_marketing/promotional_material/brochure/67/f0/0f/23/95/f2/43/d4/BRSOLAR.pdf/files/BRSOLAR.pdf/jcr:content/translations/en.BRSOLAR.pdf

[8] Harry Wirth, Karl-Anders Weiβ, Cornelia Wiesmeier, "Photovoltaic Modules : Technology and Reliability", Publisher: De Gruyter, Jan. 2016.

[9] *IEEE Standard for interconnecting Distributed Resources with Electric Power Systems*, IEEE Standard 1547, 2003.

[10] "Advanced Inverter Functions to Support High Levels of Distributed Solar: Policy and Regulatory Considerations," National Renewable Energy Laboratory. Golden, CO, NREL Report No. BR-6A20-62612, Nov. 2014

[11] J. Rocabert, A. Luna, F. Blaabjerg and P. Rodriguez, "Control of Power Converters in AC Microgrids," *IEEE Transactions on Power Electronics*, vol. 27, no. 11, pp. 4734-4749, 2012.

[12] F. Blaabjerg, R. Teodorescu, M. Liserre and A. Timbus, "Overview of Control and Grid Synchronization for Distributed Power Generation Systems," *IEEE Trans. Ind. Electron.*, vol. 53, no. 5, pp. 1398-1409, 2006.

[13] W. Lenwari, "Review of a High Performance Control of AC Signals Based on a Proportional Plus Resonant Compensator," *Suranaree Journal of Science and Technology*, vol. 15, no. 4, pp. 333-344, Oct-Dec. 2008.

[14] R. Leyva, C. Olalla, H. Zazo, C. Cabal, A. Cid-Pastor, I. Queinnec, C. Alonso, "MPPT based on sinusoidal extremum-seeking control in PV generation, " *International Journal of Photoenergy*, vol. 2012, pp. 672765-1-672765-7, 2012.

[15] R. Teodorescu, F. Blaabjerg, M. Liserre and P. Loh, "Proportional-resonant controllers and filters for grid-connected voltage-source converters," *IEE Proceedings - Electric Power Applications*, vol. 153, no. 5, p. 750, 2006.

[16] D. Holmes, T. Lipo, B. McGrath and W. Kong, "Optimized Design of Stationary Frame Three Phase AC Current Regulators," *IEEE Transactions on Power Electronics*, vol. 24, no. 11, pp. 2417-2426, 2009.

[17] S. Fukuda and T. Yoda, "A novel current-tracking method for active filters based on a sinusoidal internal model," *IEEE Transactions on Industry Applications*, vol. 37, no. 3, pp. 888-895, 2001.

[18] A. Timbus, M. Liserre, R. Teodorescu, P. Rodriguez and F. Blaabjerg, "Evaluation of Current Controllers for Distributed Power Generation Systems," *IEEE Transactions on Power Electronics*, vol. 24, no. 3, pp. 654-664, 2009.

[19] M. Su, P. Pan, X. Long, Y. Sun and J. Yang, "An Active Power-Decoupling Method for Single-Phase AC-DC Converters," *IEEE Transactions on Industrial Informatics*, vol. 10, no. 1, pp. 461-468, 2014.

[20] F. Gonzalez-Espin, G. Garcera, I. Patrao and E. Figueres, "An Adaptive Control System for Three-Phase Photovoltaic Inverters Working in a Polluted and Variable Frequency Electric Grid," *IEEE Transactions on Power Electronics*, vol. 27, no. 10, pp. 4248-4261, 2012.

[21] Y. Yang, K. Zhou and F. Blaabjerg, "Enhancing the Frequency Adaptability of Periodic Current Controllers with a Fixed Sampling Rate for Grid-Connected Power Converters," *IEEE Transactions on Power Electronics*, pp. 1-1, 2015.

[22] A. Timbus, M. Ciobotaru, R. Teodorescu and F. Blaabjerg, "Adaptive Resonant Controller for Grid-Connected Converters in Distributed Power Genaration Systems," in *Twenty-First Annual IEEE Applied Power Electronics Conference and Exposition*, 2006.

[23] Y. Yang, K. Zhou, H. Wang, F. Blaabjerg, D. Wang and B. Zhang, "Frequency Adaptive Selective Harmonic Control for Grid-Connected Inverters," *IEEE Transactions on Power Electronics*, vol. 30, no. 7, pp. 3912-3924, 2015.

[24] F. Gonzalez-Espin, E. Figueres and G. Garcera, "An Adaptive Synchronous-Reference-Frame Phase-Locked Loop for Power Quality Improvement in a Polluted Utility Grid," *IEEE Trans. Ind. Electron.*, vol. 59, no. 6, pp. 2718-2731, 2012.

[25] A. Monter, E. Bueno, A. Garcia-Cerrada, F. Rodriguez and F. Sanchez, "Detailed analysis of the implementation of frequency-adaptive resonant and repetitive current controllers for grid-connected converters," *Electric Power Systems Research*, vol. 116, pp. 231-242, 2014.

[26] D. Chen, J. Zhang, and Z. Qian, "An improved repetitive control scheme for grid-connected inverter with frequency-adaptive capability," *IEEE Trans. Ind. Electron.*, vol. 60, no. 2, pp. 814-823, Feb. 2013

[27] J. He, Y. Li, and F. Blaabjerg, "Flexible microgrid power quality enhancement using adaptive hybrid voltage and current controller," *IEEE Trans. Ind. Electron.* , vol. 61, no. 6, pp. 2784-2794, Jun. 2014.

[28] S. G. Jorge, C. a. Busada and J. Solsona, "Frequency-Adaptive current controller for three-phase grid-connected converters" *IEEE Trans. Ind. Electron.*, vol. 60, no. 10, pp. 4169-4177, 2013

[29] Y. Yang, L. Hadjidemetriou, F. Blaabjerg and E. Kyriak, "Benchmarking Of Phase Locked Loop Based Synchronization Techniques For Grid-Connected Inverter Systems," *9th International Conference on Power Electronics and ECCE Asia (ICPE-ECCE Asia)*, 2015.

[30] D. Llano and R. McMahon, "Single phase grid integration of permanent magnet generators associated with a wind turbine emulator test-rig," *40th Annual Conference of the IEEE Industrial Electronics Society (IECON 2014)*, Dallas, TX, 2014.

[31] S. Moura and Y. Chang, "Lyapunov-based switched extremum seeking for photovoltaic power maximization," *Control Engineering Practice*, vol. 21, no.7, pp. 971-980, 2013.

[32] K. Modyski, K. Rafa, and M. Bobrowska-Rafa, "Application of the second order generalized integrator in digital control systems," *Archives of Electrical Engineering*, vol. 63, no. 3, 2014.

[33] K. Ariyur and M. Krstic, *Real time Optimization by Extremum seeking Control.*, Wiley Interscience, Hoboken, NJ, 2003.

[34] M. Karimi-Ghartemani, "Universal Integrated Synchronization and Control for Single Phase DC/AC Converters," *IEEE Transactions on Power Electronics*, vol. 30, no. 3, pp. 1544-1557, 2015.

[35] Quan Quan and Kai-Yuan Cai, "A new viewpoint on the internal model principle and its application to periodic signal tracking," *the 8th World Congress on Intelligent Control and Automation*, pp. 1162-1167, Shandong, China, 2010.

[36] S. Khajehoddin, M. Karimi Ghartemani, P. Jain and A. Bakhshai, "A Resonant Controller With High Structural Robustness for Fixed-Point Digital Implementations," *IEEE Transactions on Power Electronics*, vol. 27, no. 7, pp. 3352-3362, 2012.

[37] A. Yepes, F. Freijedo, J. Doval-Gandoy, O. Lopez, J. Malvar and P. Fernandez-Comesana, “Effects of Discretization Methods on the Performance of Resonant Controllers," *IEEE Transactions on Power Electronics*, vol. 25, no. 7, pp. 1692-1712, 2010.

[38] A. Uphues, K. Notzold, R. Wegener and S. Soter, "Frequency adaptive PR-controller for compensation of current harmonics," *IEEE Industrial Electronics Society, 40th Annual Conference of the IEEE Industrial Electronics Society (IECON 2014)*, Dallas, TX, 2014.

[39] M. Castilla, J. Miret, J. Matas, L. G. de Vicuna, and J. M. Guerrero, “Linear current control scheme with series resonant harmonic compensator for single-phase grid-connected photovoltaic inverters," *IEEE Trans. Ind. Electron.*, vol. 55, pp. 2724-2733, Jul 2008.

[40] M. Habibullin, V. Pikalov, V. Mescheryakov and S. Valtchev, "Active power filter with common DC link for compensation of harmonic distortion in power grids," *16th International Power Electronics and Motion Control Conference and Exposition*, 2014.

[41] Yan Guo, and Guang Zeng. "A Digital Phase Locked Loop Based On Frequency Self-Adaptive," *IEEE 2nd International Future Energy Electronics Conference (IFEEC)*, 2015.

[42] L. Hadjidemetriou, Y. Yang, E. Kyriakides and F. Blaabjerg, "A Synchronization Scheme for Single-Phase Grid-Tied Inverters under Harmonic Distortion and Grid Disturbances," *IEEE Transactions on Power Electronics*, pp. 1-1, 2016.

[43] P. Rodriguez, J. Pou, J. Bergas, I. Candela, R. Burgos and D. Boroyevic, "Double Synchronous Reference Frame PLL for Power Converters Control," *IEEE 36th Conference on Power Electronics Specialists*, 2005.

[44] P. Rodriguez, A. Luna, M. Ciobotaru, R. Teodorescu and F. Blaabjerg, "Advanced Grid Synchronization System for Power Converters under Unbalanced and Distorted Operating Conditions," *IECON 2006 - 32nd Annual Conference on IEEE Industrial Electronics*, 2006.

[45] L. Arruda, S. Silva and B. Filho, "PLL structures for utility connected systems," *Conference Record of the 2001 IEEE Industry Applications Conference.* 36th IAS Annual Meeting (Cat. No.01CH37248).

[46] R. J. Ferreira, R. E. Araujo, and J. A. Pecas Lopes, "A comparative analysis and implementaion of various PLL techniques applied to singlephase grids," *International Youth Conference on Energetics (IYCE)*, Jul. 2011, pp. 1-8.

[47] F. Freijedo, J. Doval-Gandoy, O. Lopez and E. Acha, "Tuning of Phase-Locked Loops for Power Converters Under Distorted Utility Conditions," *IEEE Transactions on Industry Applications*, vol. 45, no. 6, pp. 2039-2047, 2009.

[48] Ali Elrayyah, Ali Safayet, Yilmaz Sozer, Iqbal Husain, Malik Elbuluk, "Novel Harmonic and Phase Estimator for Grid-Connected Renewable Energy Systems, " *Energy Conversion Congress and Exposition (ECCE)*, pp. 4683-4689, September 2012.

[49] S. Golestan, J. Guerrero, A. Vidal, A. Yepes, J. Doval-Gandoy and F. Freijedo, "Small-Signal Modeling, Stability Analysis and Design Optimization of Single-Phase Delay-Based PLLs," *IEEE Transactions on Power Electronics*, vol. 31, no. 5, pp. 3517-3527, 2016.

[50] R. Chattopadhyay, A. De and S. Bhattacharya, "Comparison of PR controller and damped PR controller for grid current control of LCL filter based grid-tied inverter under frequency variation and grid distortion," *2014 IEEE Energy Conversion Congress and Exposition (ECCE)* , 2014.

[51] E. Twining and D. Holmes, "Grid current regulation of a three-phase voltage source inverter with an LCL input filter," *IEEE 33rd Annual IEEE Power Electronics Specialists Conference*, Proceedings (Cat. No.02CH37289), 2002.

[52] Yaoqin Jia, Jiqian Zhao and Xiaowei Fu, "Direct Grid Current Control of LCL-Filtered Grid-Connected Inverter Mitigating Grid Voltage Disturbance," *IEEE Transactions on Power Electronics*, vol. 29, no. 3, pp. 1532-1541, 2014.

[53] "National Grid: Real Time Frequency Data - Last 60 Minutes". [Online]. available: `Nationalgrid.com`, Access-time: 31 Dec. 2016.

[54] D. Holmes and T. Lipo, *Pulse Width Modulation for Power Converters*, 1st ed. Hoboken, NJ: John Wiley, 2003

[55] X. Pei, W. Zhou and Y. Kang, "Analysis and Calculation of DC-Link Current and Voltage Ripples for Three-Phase Inverter With Unbalanced Load," *IEEE Transactions on Power Electronics*, vol. 30, no. 10, pp. 5401-5412, 2015.

[56] L. Sun, W. Zhenxing, M. Weiming, F. Xiao, X. Cai and L. Zhou, "Analysis of the DC-Link Capacitor Current of Power Cells in Cascaded H-Bridge Inverters for High-Voltage Drives," *IEEE Transactions on Power Electronics*, vol. 29, no. 12, pp. 6281-6292, 2014.

[57] N. Ninad and L. Lopes, "Operation of Single-phase Grid-Connected Inverters with Large DC Bus Voltage Ripple," *IEEE Canada Electrical Power Conference*, 2007.

[58] H. Fanbo, Z. Zhengming, Y. Liqiang, and L. Sizhao, "A DC-link voltage control scheme for single-phase grid-connected PV inverters," *Energy Conversion Congress and Exposition (ECCE),* 2011, pp. 3941-3945.

[59] H. Haibing, S. Harb, N. Kutkut, I. Batarseh, and Z. J. Shen, "Power decoupling techniques for micro-inverters in PV systems-A review," *Proc. Energy Conversion Congress and Exposition (ECCE)*, 2010 IEEE, 2010, pp. 3235-3240.

[60] F. Wang, M. Benhabib, J. Duarte and M. Hendrix, "High Performance Stationary Frame Filters for Symmetrical Sequences or Harmonics Separation Under a Variety of Grid Conditions," *Twenty-Fourth Annual IEEE Applied Power Electronics Conference and Exposition*, 2009.

[61] J. Matas, M. Castilla, J. Miret, L. Garcia de Vicuna and R. Guzman, "An Adaptive Prefiltering Method to Improve the Speed/Accuracy Tradeoff of Voltage Sequence Detection Methods Under Adverse Grid Conditions," *IEEE Trans. Ind. Electron.* , vol. 61, no. 5, pp. 2139-2151, 2014.

[62] P. Rodridguez, A. Luna, I. Candela, R. Mujal, R. Teodorescu, and F. Blaabjerg, "Multiresonant frequency-locked loop for grid synchronization of power converters under distorted grid conditions," *IEEE Trans. Ind. Electron.* , vol. 58, no. 1, pp. 127-138, Jan 2011.

Appendix A

RK4 Code

In this section, the Matlab code used to discretize/implement the proposed FLL controller is provided as sample code for how RK4 algorithm is implemented. It should be noted that the Matlab Embedded Coder is used to implement the controller. the following code was used in an embedded Matlab function.

A.1 FLL with Two Harmonic Damping Filter

```
function  [y,f] = fcn(u)

%In this function, y is the estimated phase and f is the estimated
%frequency of the grid. input is the normalized grid voltage

% 1. defining the dynamic system states as follows:

persistent x1; persistent x2; persistent x3;persistent x4;persistent x5;
persistent x6;persistent x7;persistent x8;persistent x9;persistent x10;


% 2. defining two flags to determine the flow of program:

persistent flag; persistent init_flag;

% 3. defining the components of RK4 algorithm for each state:

persistent v1_x1; persistent v2_x1; persistent v3_x1; persistent v4_x1;
persistent v1_x2; persistent v2_x2; persistent v3_x2; persistent v4_x2;
persistent v1_x3; persistent v2_x3; persistent v3_x3; persistent v4_x3;
persistent v1_x4; persistent v2_x4; persistent v3_x4; persistent v4_x4;
persistent v1_x5; persistent v2_x5; persistent v3_x5; persistent v4_x5;
persistent v1_x6; persistent v2_x6; persistent v3_x6; persistent v4_x6;
persistent v1_x7; persistent v2_x7; persistent v3_x7; persistent v4_x7;
```

```
persistent v1_x8; persistent v2_x8; persistent v3_x8; persistent v4_x8;
persistent v1_x9; persistent v2_x9; persistent v3_x9; persistent v4_x9;
persistent v1_x10; persistent v2_x10; persistent v3_x10; persistent v4_x10;

% 4. defining the values of output in the mid-points
     % where states are not updated:

persistent y_middle;persistent f_middle;


% 5. defining the values of the controller parameters:

T=1/(120*60); %discrete step-time
K=200; %resonant filter gain
a=2; %extremum-seeking perturbation amplitude
K_ecs=-125000; %extremum-seeking gain
wn_b = 2*pi*120; %extremum-seeking notch filter resonant frequency
zig = 2; % extremum-seeking notch filter damping factor
zig1 = 0.1; %the damping factor of first harmonic damping notch filter
zig2 = 0.1; %the damping factor of second harmonic damping notch filter

% 6. Initialization of variables:

if isempty(x1)
   x1 = 0;
end
if isempty(x2)
   x2 = 0;
end
if isempty(x3)
   x3 = 60;
end

...

if isempty(x10)
   x10 = 0;
end
if isempty(flag)
   flag = 0;
end
if isempty(init_flag)
   init_flag = 1;
end
if isempty(v1_x1)
   v1_x1 = 0;
end
```

```
if isempty(v1_x2)
   v1_x2 = 0;
end
if isempty(v1_x3)
   v1_x3 = 0;
end

...

if isempty(v1_x10)
   v1_x10 = 0;
end

...

if isempty(v4_x9)
   v4_x9 = 0;
end
if isempty(v4_x10)
   v4_x10 = 0;
end
if isempty(y_middle)
   y_middle = 0;
end
if isempty(f_middle)
   f_middle = 0;
end


% The adaptive resonant frequency of harmonic damping notch filters:
omg1 = 2*pi*x3*2;
omg2 = 2*pi*x3*3;

% 7. Estimation of Next states:

if (flag==0) %if it is not a mid-point calculation
    if (init_flag==1) %if it is initialization

        y = x2;
        f = abs(x3);
        y_middle = y;
        f_middle = f;

        v1_x1 = x2;
        v1_x2 = (u-x2-x10-x8)*K-x1*(2*pi*(x3+a*sin(x6)))^2;
        v1_x3 = 2*((u-x2-x10-x8)^2-x5)*sin(x6)*K_ecs;
        v1_x4 = x5;
```

```
    v1_x5 = 2*zig*wn_b*(u-x2-x10-x8)^2 - wn_b*wn_b*x4 - 2*zig*wn_b*x5;
    v1_x6 = 2*pi*500;
    v1_x7 = x8;
    v1_x8 = zig2*omg2*(u-x2-x10)-omg2*zig2*x8-omg2*omg2*x7;
    v1_x9 = x10;
    v1_x10 = zig1*omg1*(u-x2)-omg1*zig1*x10-omg1*omg1*x9;


elseif (init_flag==0) %if it is not initialization
    y = x2;
    f=abs(x3);
    y_middle = y;
    f_middle = f;

    %last component of rk4 is calculated:

    v4_x1 =  x2+T*v3_x2;
    v4_x2 = (u-(x2+T*v3_x2)-(x10+T*v3_x10)-(x8+T*v3_x8))*K
             -(x1+T*v3_x1)*(2*pi*((x3+T*v3_x3)+a*sin(x6+T*v3_x6)))^2;
    v4_x3 = 2*((u-(x2+T*v3_x2)-(x10+T*v3_x10)-(x8+T*v3_x8))^2
             -(x5+T*v3_x5))*sin(x6+T*v3_x6)*K_ecs;
    v4_x4 = x5 + T*v3_x5;
    v4_x5 = 2*zig*wn_b*(u-(x2+T*v3_x2)-(x10+T*v3_x10)-(x8+T*v3_x8))^2
             - wn_b*wn_b*(x4+T*v3_x4) - 2*zig*wn_b*(x5+T*v3_x5);
    v4_x6 = 2*pi*500;
    v4_x7 = x8+T*v3_x8;
    v4_x8 = zig2*omg2*(u-(x2+T*v3_x2)-(x10+T*v3_x10))
             -omg2*zig2*(x8+T*v3_x8)-omg2*omg2*(x7+T*v3_x7);
    v4_x9 = x10+T*v3_x10;
    v4_x10 = zig1*omg1*(u-(x2+T*v3_x2))-omg1*zig1*(x10+T*v3_x10)
              -omg1*omg1*(x9+T*v3_x9);

     % states are updated:
    x1 = x1 +   (T/6)*(v1_x1+2*v2_x1+2*v3_x1+v4_x1);
    x2 = x2 +   (T/6)*(v1_x2+2*v2_x2+2*v3_x2+v4_x2);
    x3 = x3 +   (T/6)*(v1_x3+2*v2_x3+2*v3_x3+v4_x3);
    x4 = x4 +   (T/6)*(v1_x4+2*v2_x4+2*v3_x4+v4_x4);
    x5 = x5 +   (T/6)*(v1_x5+2*v2_x5+2*v3_x5+v4_x5);
    x6 = x6 +   (T/6)*(v1_x6+2*v2_x6+2*v3_x6+v4_x6);
    x7 = x7 +   (T/6)*(v1_x7+2*v2_x7+2*v3_x7+v4_x7);
    x8 = x8 +   (T/6)*(v1_x8+2*v2_x8+2*v3_x8+v4_x8);
    x9 = x9 +   (T/6)*(v1_x9+2*v2_x9+2*v3_x9+v4_x9);
    x10 = x10 + (T/6)*(v1_x10+2*v2_x10+2*v3_x10+v4_x10);

    % the first component of the next-state is calculated:

    v1_x1 = x2;
```

```
        v1_x2 = (u-x2-x10-x8)*K-x1*(2*pi*(x3+a*n*sin(x6)))^2;
        v1_x3 = 2*((u-x2-x10-x8)^2-x5)*sin(x6)*K_ecs;
        v1_x4 = x5;
        v1_x5 = 2*zig*wn_b*(u-x2-x10-x8)^2 - wn_b*wn_b*x4 - 2*zig*wn_b*x5;
        v1_x6 = 2*pi*500;
        v1_x7 = x8;
        v1_x8 = zig2*omg2*(u-x2-x10)-omg2*zig2*x8-omg2*omg2*x7;
        v1_x9 = x10;  %first notch from the u-x2
        v1_x10 = zig1*omg1*(u-x2)-omg1*zig1*x10-omg1*omg1*x9;


         else
         y=0;
         f=0;
    end
elseif (flag==1)    % if it is mid-point calculation

    y = y_middle;   %output values are kept
    f = f_middle;


    v2_x1 = x2+(T/2)*v1_x2;
    v2_x2 = (u-(x2+(T/2)*v1_x2)-(x10+(T/2)*v1_x10)-(x8+(T/2)*v1_x8))*K
          -(x1+(T/2)*v1_x1)*(2*pi*((x3+(T/2)*v1_x3)
          +a*sin(x6+(T/2)*v1_x6)))^2;
    v2_x3 = 2*((u-(x2+(T/2)*v1_x2)-(x10+(T/2)*v1_x10)-(x8+(T/2)*v1_x8))^2
          -(x5+(T/2)*v1_x5))*sin(x6+(T/2)*v1_x6)*K_ecs;
    v2_x4 = x5 + (T/2)*v1_x5;
    v2_x5 = 2*zig*wn_b*(u-(x2+(T/2)*v1_x2)-(x10+(T/2)*v1_x10)
          -(x8+(T/2)*v1_x8))^2 - wn_b*wn_b*(x4+ (T/2)*v1_x4)
          - 2*zig*wn_b*(x5+(T/2)*v1_x5);
    v2_x6 = 2*pi*500;
    v2_x7 = x8+(T/2)*v1_x8; %second notch to the pr
    v2_x8 = zig2*omg2*(u-(x2+(T/2)*v1_x2)-(x10+(T/2)*v1_x10))
          -omg2*zig2*(x8+(T/2)*v1_x8)-omg2*omg2*(x7+(T/2)*v1_x7);
    v2_x9 = x10+(T/2)*v1_x10;
    v2_x10 = zig1*omg1*(u-(x2+(T/2)*v1_x2))-omg1*zig1*(x10+(T/2)*v1_x10)
           -omg1*omg1*(x9+(T/2)*v1_x9);



    v3_x1= x2+(T/2)*v2_x2;
    v3_x2 = (u-(x2+(T/2)*v2_x2)-(x10+(T/2)*v2_x10)-(x8+(T/2)*v2_x8))*K
          -(x1+(T/2)*v2_x1)*(4*pi*pi*((x3+(T/2)*v2_x3)
          +a*sin(x6+(T/2)*v2_x6)))^2;
    v3_x3 = 2*((u-(x2+(T/2)*v2_x2)-(x10+(T/2)*v2_x10)-(x8+(T/2)*v2_x8))^2
          -(x5+(T/2)*v2_x5))*sin(x6+(T/2)*v2_x6)*K_ecs;
```

```
    v3_x4 = x5 + (T/2)*v2_x5;
    v3_x5 = 2*zig*wn_b*(u-(x2+(T/2)*v2_x2)-(x10+(T/2)*v2_x10)
            -(x8+(T/2)*v2_x8))^2 - wn_b*wn_b*(x4+ (T/2)*v2_x4)
            - 2*zig*wn_b*(x5+(T/2)*v2_x5);
    v3_x6 = 2*pi*500;
    v3_x7 = x8+(T/2)*v2_x8;
    v3_x8 = zig2*omg2*(u-(x2+(T/2)*v2_x2)-(x10+(T/2)*v2_x10))
            -omg2*zig2*(x8+(T/2)*v2_x8)-omg2*omg2*(x7+(T/2)*v2_x7);
    v3_x9 = x10+(T/2)*v2_x10;
    v3_x10 = zig1*omg1*(u-(x2+(T/2)*v2_x2))-omg1*zig1*(x10+(T/2)*v2_x10)
             -omg1*omg1*(x9+(T/2)*v2_x9);
else
     y=0;
     f=0;
end

% 8. Change the flag to calculate mid-points/main-points in
     % the next computation cycle:

if(flag==1)
    flag=0;
elseif(flag==0)
    flag=1;
end


% 9. Turn off the initialization flag after one computation step-time:

if(init_flag==1)
    init_flag=0;
end
```